Marine and Petroleum Geology 167 (2024) 106959

Contents lists available at ScienceDirect

Marine and Petroleum Geology

journal homepage: www.elsevier.com/locate/marpetgeo

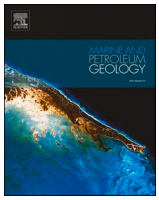

Geochemistry and accumulation of the ultra-deep Ordovician oils in the Shunbei oilfield, Tarim Basin: Coupling of reservoir secondary processes and filling events

Rongzhen Qiao, Meijun Li *, Donglin Zhang, Hong Xiao

National Key Laboratory of Petroleum Resources and Engineering, College of Geosciences, China University of Petroleum (Beijing), Beijing, 102249, China

ARTICLE INFO

Keywords:
Geochemical characteristics
Biodegradation
Thermal alteration
Mixing
Evaporative fractionation
Accumulation process

ABSTRACT

Ultra-deep (7300 m–8900 m) condensed and volatile oil reservoirs have been discovered in the Ordovician reservoirs of the Shunbei oilfield, in the Tarim Basin. This study describes the petroleum accumulation process in the Shunbei oilfield by combining an analysis of its geochemical characteristics with seismic section observations and an analysis of petroleum filling events. Geochemical techniques are used to determine the sources, maturity, secondary processes, accumulation periods, and timing of petroleum filling. Analysis of fluid inclusion homogenization temperatures and burial-thermal histories indicates distinct petroleum filling events. Specifically, the north sub-section of the No. 5 fault zone experienced two petroleum filling periods during the late Caledonian and Indosinian epochs while the No. 1 fault zones and the mid-south sub-sections of the No. 5 fault zones experienced three distinct filling periods, encompassing the late Caledonian, Indosinian, and Himalayan periods. The CO_2 concentrations and $\delta^{13}C_{CO2}$ values suggest the presence of secondary microbial gases, primarily thermogenic gases. Gas component analysis reveals a transition from kerogen degradation gas to oil cracking gas from north to south. The detection of intact *n*-alkanes and compounds of the 25-norhopanes series in oil samples suggests a mixture of early biodegradable oil with late fresh oil in the area. Seismic sections reveal diabase intrusions with strong axial reflections. Local hydrothermal activities during the Permian era rapidly cracked saturated hydrocarbon biomarkers, forming polycyclic aromatic hydrocarbons in the oil. Hydrothermal activity in the south sub-section of the No. 5 fault zone depleted the hydrocarbon-generating capacity of the underlying source rocks. Petroleum charged during the Indosinian period likely originated from potential petroleum reservoirs in the Cambrian system. This explains the comparatively low temperature of the SHB57X reservoir (163.32 °C) and the lack of strong hydrothermal activity in the late stage, but no biomarkers of the second-stage charged oil have been detected. Biomarker detection and gas genesis in the mid-south sub-section of the No. 5 fault zone and in the No. 1 fault zone suggest weak or no hydrothermal activity, with Cambrian source rocks maintaining their hydrocarbon generation capacity. Gas filling in the Himalayan period caused evaporative fractionation in the original reservoirs, resulting in a disproportionate (2-MH+2,3-DMP)/(3-MH+2,4-DMP), producing high K1 values in the light hydrocarbons in the present petroleum reservoirs. Differences in gas charging events in the Himalayan period led to the present distribution of petroleum phases.

1. Introduction

The global petroleum industry, driven by advances in drilling technology, is progressively venturing into deep and ultra-deep fields (reservoir depths >4500 m) (Dyman et al., 2002). Well O-14 in Russia's Chayvo oilfield has been drilled to 13,500 m. Deep and ultra-deep petroleum exploration has achieved major breakthroughs in major basins around the world. In countries with a high degree of deep exploration, such as Mexico, Italy, and the United States, proven deep petroleum reserves now exceed 39% of their total reserves (Yao et al., 2018). This trend underscores the immense potential of deep and ultra-deep reservoirs within basins, which will be crucial contributors to global petroleum resources.

China's current deep and ultra-deep petroleum exploration focuses predominantly on carbonate reservoirs within the superimposed basins of the central and western regions. For example, the Ordovician

* Corresponding author.
E-mail address: meijunli@cup.edu.cn (M. Li).

https://doi.org/10.1016/j.marpetgeo.2024.106959
Received 14 February 2024; Received in revised form 11 June 2024; Accepted 12 June 2024
Available online 14 June 2024

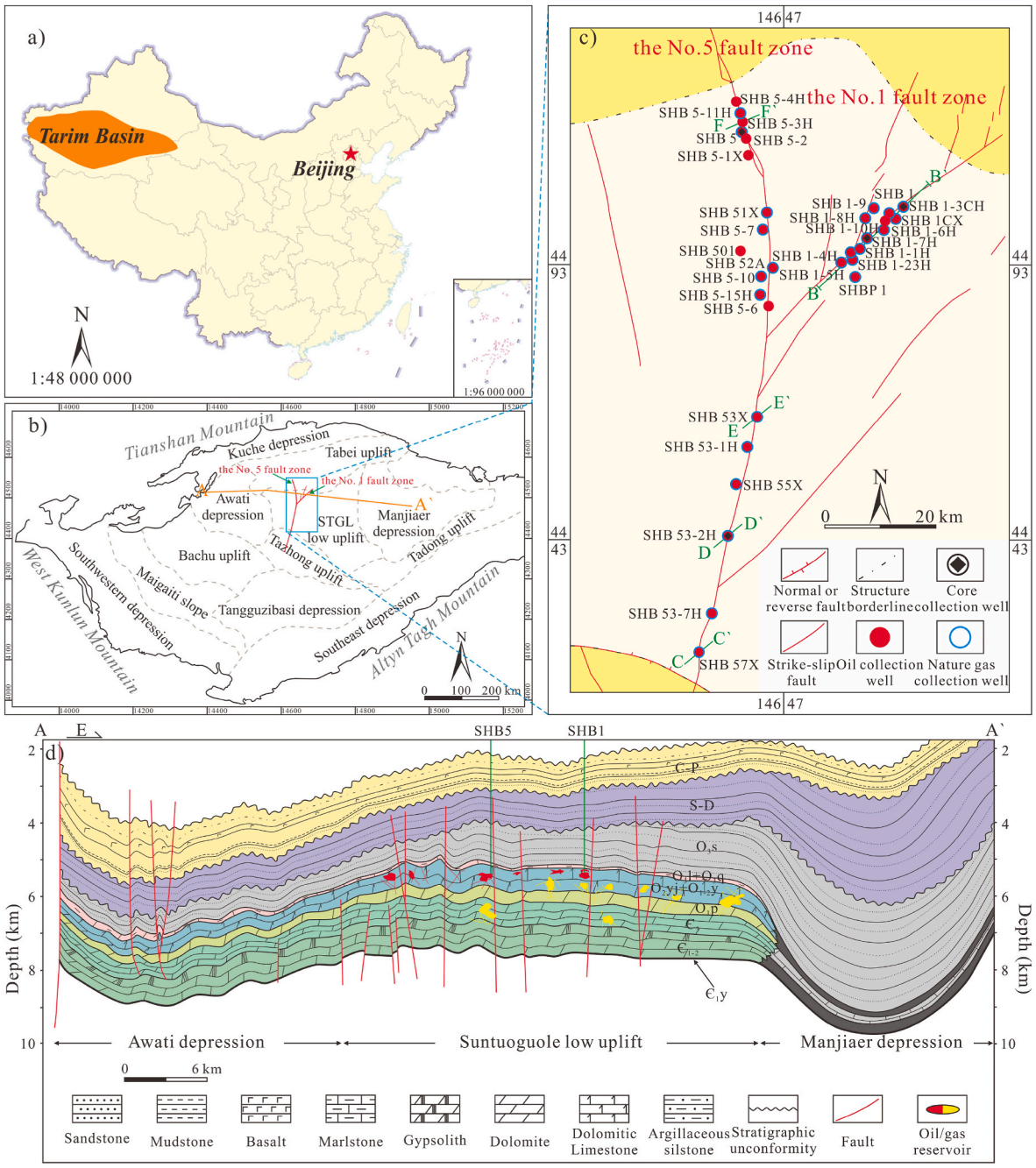

Fig. 1. a) Map showing the location of the Tarim Basin; b) Map showing tectonic divisions and location of the study area in the Tarim Basin; c) Map showing locations of the sampled wells; d) Geological cross section A-A′ across the Awati depression, the STGL low uplift, and the Manjiaer depression. The A-A′ is a geological cross section (Fig. 1d) crossing the Central Tarim area. The B–B′ is a seismic section (Fig. 8) crossing the No. 1 fault zones. The C–C′, D-D′, E-E′, and F–F′are seismic sections (Fig. 9) that pass through SHB57X, SHB53–2H, SHB53X, and SHB5–3H, respectively.

dolomite reservoir in the Ordos Basin and the Sinian dolomite reservoir in the Sichuan Basin have witnessed a series of natural gas breakthroughs (Du et al., 2019; Fang et al., 2024). Exploration for liquid hydrocarbons, including black oil, normal oil, light oil, volatile oil, and condensate, in the Paleozoic and Proterozoic carbonate reservoirs in the Tarim Basin is therefore of paramount significance. Recent drilling made a groundbreaking achievement in well TS5, where the oldest formation containing liquid hydrocarbons is the dolomite of the Upper Sinian Qigebulak Formation (Z_2q), which has a reservoir temperature of 176 °C (Cao et al., 2024). This not only extends the lower limit of liquid hydrocarbon occurrence but also affirms the resource potential of ultra-deep petroleum exploration in the Tarim Basin.

Over the past two decades, there has been considerable debate regarding the origin of the petroleum in the Paleozoic reservoirs of the Tarim Basin. Some studies have proposed that the Middle-Upper Ordovician (O_{2-3}) source rocks are the primary contributors based on biomarkers and carbon isotope evidence (Li et al., 2010a, 2015). However, conventional biomarkers and carbon isotope data are not suitable for oil-source correlation in the Tarim Basin due to the distortion caused by secondary processes (Cai et al., 2009a). Furthermore, extensive drilling and source rock evaluations have revealed deficiencies in O_{2-3} large-scale effective source rocks. Sulfur isotope evidence confirms the involvement of Cambrian (Є) source rocks in the petroleum in the Paleozoic reservoirs in the Tarim Basin (Cai et al., 2009a, 2009b, 2015).

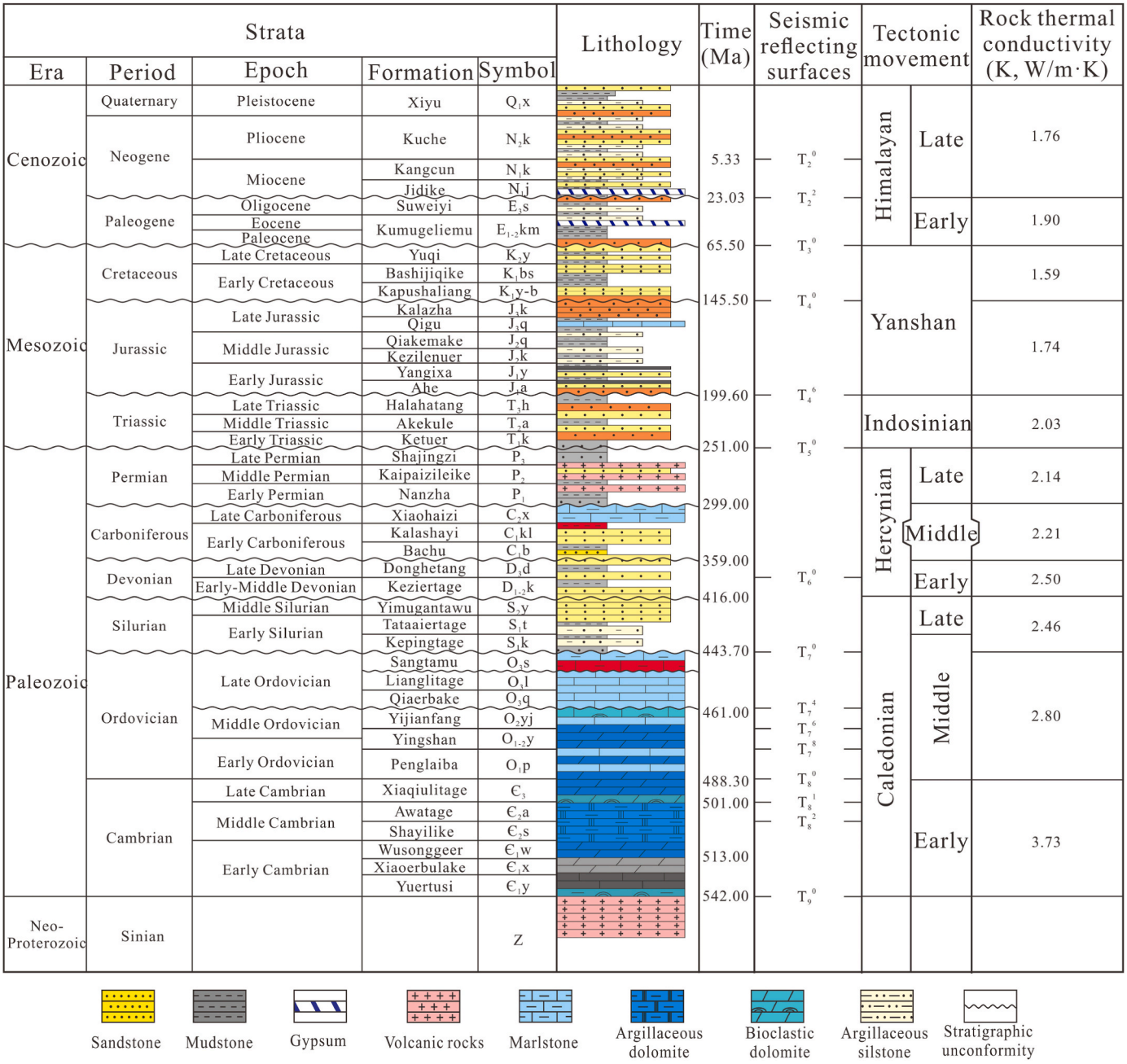

Fig. 2. Generalized stratigraphy columns of the Shunbei oilfield, Tarim Basin. Thermal conductivity (K) data are from Liu et al. (2015); stratigraphic age date and seismic reflecting surfaces division are from SINOPEC Northwest Company (Urumqi).

Additionally, investigations in Wells LT1, XH1, and TS5 have confirmed that the Cambrian Yuertusi Formation (ϵ_1y) mudstone is the primary petroleum source rock in the basin (Zhu et al., 2020, 2021; Wang et al., 2023; Cao et al., 2024).

The Shunbei oilfield is a crucial petroleum area in the Tarim Basin. Outcrops, well profiles, and seismic data indicate that the sedimentary facies of ϵ_1y in the Shunbei oilfield predominantly reflect a semi-deep-water to deep-water shelf environment (Zhu et al., 2020). The formation of extensive, high-quality source rocks in the study area was facilitated by the Early Cambrian global transgression and bioexplosion (Knoll and Carroll, 1999; Amthor et al., 2003; Dalziel, 2014). Previous studies have shown that the petroleum in the Shunbei oilfield is mainly derived from the source rocks of ϵ_1y (Ma et al., 2022; Bian et al., 2023). Additionally, within the Shunbei oilfield, there are regional petroleum properties that differ significantly, characterized by the overall distribution of "gas in the south, oil in the north" (Chen et al., 2021). This is the result of multiple stages of hydrocarbon generation, structural adjustments, accumulation, and secondary processes (e.g., thermal alteration and mixing) (Wang et al., 2021; Li et al., 2022a). Despite the known limitations of using molecular compounds or biomarkers in the analysis of ancient oil reservoirs (Chen et al., 2017), numerous studies have demonstrated their effectiveness for detection and application. In particular, they have proved valuable for paleo-environment reconstruction, oil-source correlation, and the identification of secondary processes (Brocks et al., 2003; Dutta et al., 2013; Schinteie and Brocks, 2014; Snowdon et al., 2016). This is particularly crucial for the precise characterization and reconstruction of petroleum accumulations (Wang et al., 2021; Qiao et al., 2022; Qiao and Chen, 2022).

This study focuses on core, gas, and oil samples from the No. 1 and No. 5 fault zones in the Shunbei oilfield. The primary reservoirs

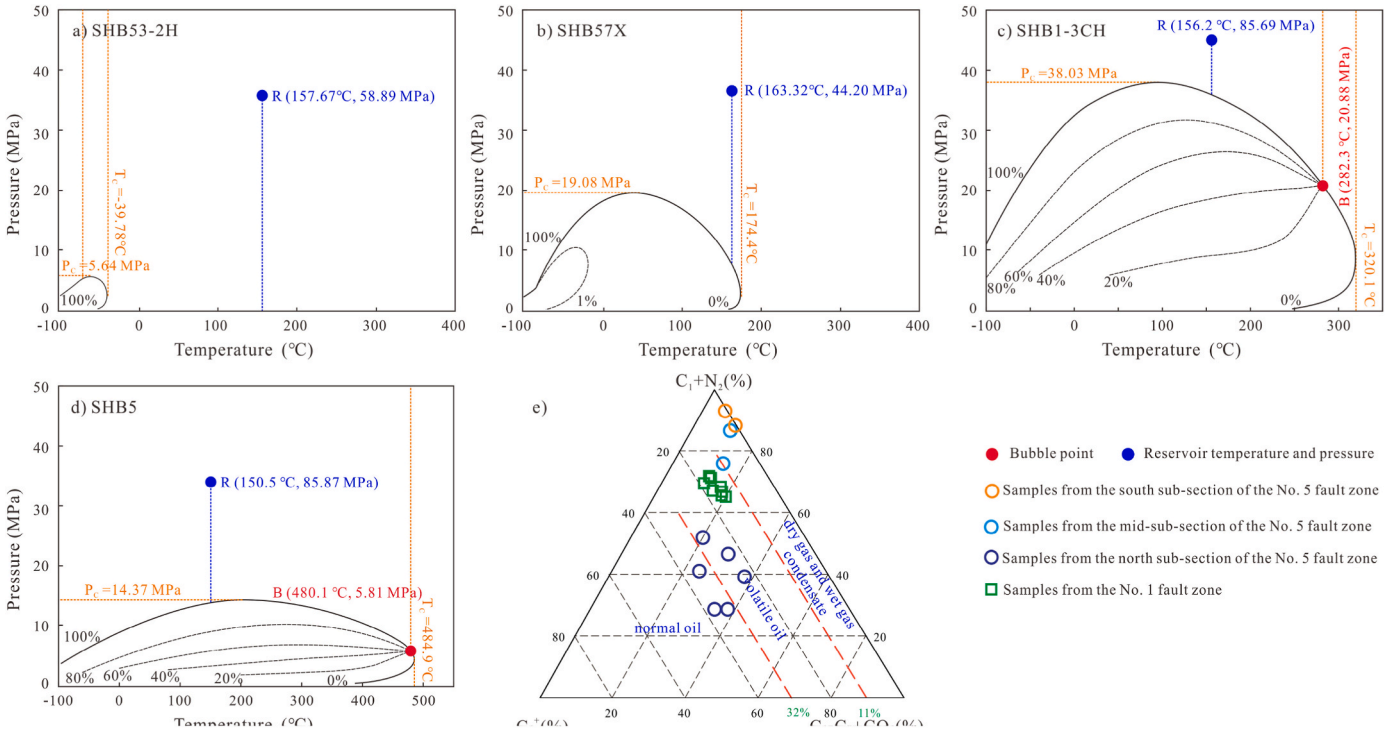

Fig. 3. PVT phase diagrams (a, b, c, d) and three-terminal diagram of fluid components (e) of the Shunbei oilfield. B = bubble point; P_C = cricondenbar; R = reservoir; T_C = cricondentherm.

investigated within the study area are in the Yingshan Formation ($O_{1\text{-}2}y$) and the Yijianfang Formation (O_2yj), using hydrocarbon molecular and stable isotopic compositions, biomarkers, and a detailed examination of hydrocarbon geochemical characteristics and genes. Combining this with the timings and periods of petroleum filling allows analysis of the impacts of various secondary processes. The objective is to utilize organic geochemical methods to develop a nuanced depiction of the hydrocarbon accumulation complexities of the Tarim Basin, offering valuable insights for the exploration of ultra-deep petroleum.

2. Geological setting

The Tarim Basin is a prototypical superimposed basin in western China, evolved on an Archean-Early Mesoproterozoic crystalline and metamorphic fold basement (Fig. 1a). Lying between the Tianshan and Kunlun orogenic belts (Li et al., 2010b), the basin's roughly diamond-shaped geomorphology is the result of the interplay between extrusion and tensional tectonic stresses (Fig. 1b). The Shunbei oilfield lies predominantly in the desert-covered area of the central basin, the Shuntuoguole Low Uplift, proximate to the Tabei Uplift, the Tazhong Uplift, the Awati Depression, and the Mangar Depression (Fig. 1b and c). The Shunbei oilfield is mainly supplied by in situ marine sources, with oil and gas primarily migrating vertically along strike-slip faults (Ma et al., 2022). The favorable structural position and abundant oil sources of the Shunbei oilfield provide excellent conditions for the long-term migration and accumulation of petroleum (Fig. 1d).

Previous studies using logging, seismic, and aeromagnetic data have found that the Tarim Basin has experienced three extension-convergence cycles during its evolution: the Sinian-Devonian, the Carboniferan-Triassic, and the Meso-Cenozoic cycles (J. Chen et al., 2022). Four major tectonic stages occurred: the early Caledonian Paleo-uplift embryonic stage, the mid-late Caledonian Early Hercynian Paleo-uplift formation stage, the late Hercynian Indochinese fault-uplift development stage, and the Yanshan-Himalayan adjustment-type stage (Fig. 2; Chen et al., 2021).

In terms of sequence stratigraphy, the Sinian-Devonian system represents a marine sequence, the Carboniferous system signifies a marine-terrestrial transitional sequence, and the Triassic system is characterized as a continental sequence. Certain local areas of the Cretaceous-Paleocene contain marine sequences (Qi, 2016). The "West Platform, East Basin" pattern in the Tarim Basin persisted from the Cambrian to the Ordovician, with the Shuntuoguole Low Uplift undergoing relatively complete sedimentation during this period. This study focuses on the Yingshan ($O_{1\text{-}2}y$) and Yijianfang Formations (O_2yj) in the Middle and Lower Ordovician. These formations are in angular unconformity contact with the upper Ordovician Series, and the Qiaerbake Formation (O_3q) is absent in some areas (Fig. 1d).

3. Samples and methods

3.1. Samples

The study focused on investigating petroleum in the Ordovician reservoirs in the No. 1 and No. 5 fault zones in the Shunbei oilfield. A comprehensive dataset comprising 25 gas, 32 oil, and 20 core samples was collected for analysis (Fig. 1c). Oil samples were analyzed using gas chromatography (GC), chromatography-mass spectrometry (GC-MS), and carbon isotopic analysis. Molecular and carbon isotopic component analyses were conducted on the natural gas samples. In addition, core samples were subjected to detailed petrological observation and inclusion homogenization temperature measurement. The natural gas and oil samples were collected directly from the wellheads, while core samples were generously provided by SINOPEC Northwest Company (Urumqi). After collection, the samples were carefully transported to the National Key Laboratory of Petroleum Resources and Engineering under stringently sealed and refrigerated conditions, and the experiments were subsequently carried out at the laboratory facilities.

3.2. Methods

3.2.1. Gas analysis

The natural gas samples were analyzed using an HP 6890 II gas

Table 1
Basic information, physical properties, and stable carbon isotope compositions of oils from the Shunbei oilfield.

Area		Well	Strate	Depth (m)		Density (g/cm^3)	Viscosity (mm^2/s)	Sulfur (%)	Wax (%)	GOR (m^3/m^3)	P_R (MPa)	T_R (°C)	$\delta^{13}C_{PDB}$, ‰				
													Oil	Sat	Aro	Res	Asp
The No.5 fault zone	south sub-section	SHB57X	$O_2yj + O_{1-2}y$	7315	7950	0.837	3.570	0.019	0.740	12734	44.20	163.32	−29.3	−29.1	−28.4	−27.9	−28.2
		SHB53–7H	$O_2yj + O_{1-2}y$	7710	8431	0.766	1.244	0.008	3.500	279807	67.81	170.63	−31.5	−31.6	−28.9	−28.0	−29.1
		SHB53–2H	$O_2yj + O_{1-2}y$	7754	8887	0.820	4.560	0.306	3.590	27533	58.89	157.67	−30.7	−30.2	−29.1	−26.9	−28.7
	mid-sub-section	SHB55X	$O_2yj + O_{1-2}y$	8050	8100	0.806	2.502	0.297	5.800	4149	76.62	169.80	−31.9	−31.9	−28.8	−27.9	−30.2
		SHB53–1H	$O_2yj + O_{1-2}y$	7731	8241	0.796	2.616	0.069	0.500	1894	43.37	171.42	−32.6	−32.6	−30.1	−29.2	−30.1
		SHB53X	$O_2yj + O_{1-2}y$	7915	8362	0.784	2.360	0.065	1.750	900	33.64	159.37	−33.0	−32.8	−31.3	−30.9	−31.6
	north sub-section	SHB5-6	$O_2yj + O_{1-2}y$	7610	7654	0.798	3.060	0.096	7.610	221	51.71	161.14	−32.3	−32.6	−30.7	−30.2	−32.1
		SHB5–15H	$O_2yj + O_{1-2}y$	7715	7842	0.809	3.510	0.090	2.220	272	51.31	161.38	−32.3	−32.6	−30.7	−30.2	−32.1
		SHB5-10	$O_2yj + O_{1-2}y$	7639	8143	0.805	3.420	0.092	6.050	269	61.84	164.97	−33.1	−32.8	−31.2	−30.6	−31.2
		SHB52A	$O_2yj + O_{1-2}y$	7891	7745	0.796	3.870	0.093	3.100	260	86.76	170.30	−32.3	−32.8	−30.8	−29.5	−32.0
		SHB501	$O_2yj + O_{1-2}y$	7740	7818	0.805	3.320	0.128	3.590	158	81.10	164.98	−32.4	−32.7	−30.4	−29.8	−31.2
		SHB5-7	$O_2yj + O_{1-2}y$	7559	7621	0.802	3.300	0.088	1.120	385	67.50	157.07	–	–	–	–	–
		SHB51X	$O_2yj + O_{1-2}y$	7684	7712	0.803	3.810	0.104	7.420	262	52.56	166.56	−32.4	−32.7	−30.8	−30.4	−31.2
		SHB5-1X	$O_2yj + O_{1-2}y$	7550	7557	0.829	6.030	0.180	3.670	281	51.38	153.74	−32.0	−32.5	−31.3	−30.4	−31.5
		SHB5-2	$O_2yj + O_{1-2}y$	–	–	0.829	6.620	0.176	1.050	–	65.74	149.75	−32.2	−32.4	−31.3	−30.5	−30.6
		SHB5	$O_2yj + O_{1-2}y$	7386	7649	0.830	4.370	0.198	4.380	64	85.87	150.50	−32.1	−32.5	−31.1	−30.1	−30.7
		SHB5–3H	$O_2yj + O_{1-2}y$	7345	7861	0.837	6.950	0.172	4.720	–	55.12	157.61	−32.6	−32.9	−31.7	−31.6	−32.3
		SHB5–11H	$O_2yj + O_{1-2}y$	7569	7710	0.840	6.980	0.240	2.460	75.3	55.71	160.27	–	–	–	–	–
		SHB5-4	$O_2yj + O_{1-2}y$	7410	7480	0.840	8.060	0.180	4.850	115	81.38	149.10	−31.7	−31.8	−30.8	−29.6	−30.5

Area	Well	Strate	Depth (m)		Density (g/cm^3)	Viscosity (mm^2/s)	Sulfur (%)	Wax (%)	GOR (m^3/m^3)	P_R (MPa)	T_R (°C)	$\delta^{13}C_{PDB}$, ‰				
												Oil	Sat	Aro	Res	Asp
The No.1 fault zone	SHB1–5H	$O_2yj + O_{1-2}y$	7474	7745	0.809	3.400	0.113	7.530	437	38.18	165.67	−32.0	−32.1	−30.1	−29.2	−29.4
	SHB1–4H	$O_2yj + O_{1-2}y$	7475	7561	0.800	2.860	0.114	5.750	292	65.37	163.07	−31.8	−32.0	−30.5	−29.3	−29.5
	SHB1–23H	$O_2yj + O_{1-2}y$	–	–	0.815	3.730	0.603	4.740	–	67.88	157.87	–	–	–	–	–
	SHB1–1H	$O_2yj + O_{1-2}y$	7613	7557	0.792	2.210	0.102	2.870	397	75.80	164.17	−32.3	−32.8	−30.7	−28.8	−29.3
	SHB1–7H	$O_2yj + O_{1-2}y$	7366	7456	0.794	2.490	0.142	2.950	465	35.31	164.78	−31.8	−32.1	−30.2	−29.5	−30.0
	SHB1–6H	$O_2yj + O_{1-2}y$	7288	7789	0.797	2.350	0.103	9.550	440	58.23	167.32	−32.0	−32.1	−30.3	−28.6	−30.1
	SHB1–8H	$O_2yj + O_{1-2}y$	7475	7534	0.795	2.500	0.086	2.100	409	56.55	161.70	−32.1	−32.4	−30.8	−30.1	−30.7
	SHB1-9	$O_2yj + O_{1-2}y$	7535	7675	0.799	3.030	0.101	2.660	442	78.02	157.47	−31.8	−32.1	−30.7	−30.5	−31.4
	SHB1–10H	$O_2yj + O_{1-2}y$	7656	7754	0.8039	2.88	0.105	2.340	498	57.75	123.86	−32.5	–	–	–	–
	SHB1CX	$O_2yj + O_{1-2}y$	7364	7470	0.795	2.150	0.146	1.860	530	64.98	157.15	−32.1	−32.4	−31.5	−30.2	−30.7
	SHB1	$O_2yj + O_{1-2}y$	7280	7407	0.790	2.230	0.106	3.930	–	74.75	151.14	−33.1	−33.2	−31.7	−28.6	−30.2
	SHB1–3CH	$O_2yj + O_{1-2}y$	7393	7440	0.794	2.490	0.111	5.590	339	85.69	156.20	−31.9	−32.0	−30.4	−29.0	−29.7
	SHBP1	$O_2yj + O_{1-2}y$	7651	7654	0.805	3.150	0.110	5.380	–	64.49	163.30	−32.4	−32.7	−31.4	−31.5	−31.7

GOR: cumulative produced gas to oil ratio; P_R: Reservoir pressure; T_R: Reservoir temperature; Sat: Saturated fractions; Aro: Aromatic fraction; Res: Resin; Asp: Asphaltene; "–": no data or not determined.

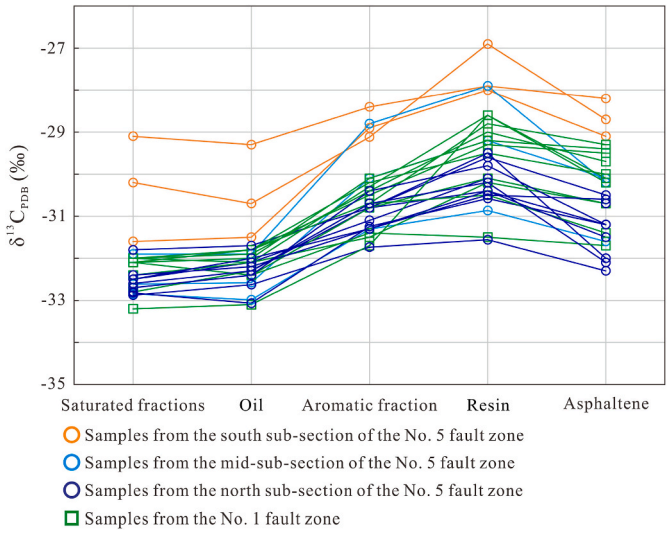

Fig. 4. Distribution of carbon isotope compositions of oils from the Shunbei oilfield.

chromatograph with flame ionization and thermal conductivity detectors. The hydrocarbon gas components were identified using gas chromatography, while the stable carbon isotopes of the gas samples were measured using GC-IRMS with a carrier coupled to the HP 6890 IIGC apparatus.

3.2.2. Oil analysis

The oil group components were separated using column chromatography, a traditional method. Each sample was divided into asphaltene, saturated hydrocarbons, aromatic hydrocarbons, and non-hydrocarbon components using elution solvents such as petroleum ether, dichloromethane, and dichloromethane + methanol.

Stable carbon isotopes ($\delta^{13}C$) of the fractions were analyzed using a FLASH 2000 EA-MAT 253 IRMS stable isotope mass spectrometer interfaced with an HP 5890II chromatograph. Combustion was initially set at 980 °C, and then adjusted to 250 °C. Liquid nitrogen was employed for cooling, purification, and collection. The isotope ratios are reported as per mil (%) deviations relative to the Vienna Pee Dee belemnite (VPDB) standard for carbon. The $\delta^{13}C$ values were calibrated with errors of less than 0.1‰.

Saturated hydrocarbons and aromatic components were analyzed by gas chromatography-mass spectrometry (GC-MS) using an Agilent 6890GC/5975i MS system. An HP-PONA column (60 m × 0.25 mm × 0.25 μm) was employed in the gas chromatograph. The analysis involved heating the gas chromatograph to 50 °C, holding for 1 min, increasing to 250 °C at a rate of 20 °C/min, and finally reaching 310 °C at a rate of 20 °C/min, where it was held for 10 min. The mass spectrometer was operated at an electron ionization energy of 70 eV in the selected ion monitoring mode. To quantify the chemicals in the saturated hydrocarbon components, known concentrations of sterane in d4-C_{29} (20 R) were used as internal standards.

The GC-MS analysis of diamondoids followed the same procedure as for the saturated hydrocarbon components. To determine the absolute concentration of diamondoids, known concentrations of d16-diamantine were added to the entire oil sample as a quantitative internal standard.

3.2.3. Phase analysis

The simulation was based on gas and oil fractions, along with key petroleum physical properties such as the gas-oil ratio (GOR) and crude oil density. PVTsim software was used to fit and normalize the fluid components. Parameters such as temperature and pressure were then set in the Interfaces module. Finally, simulations of the petroleum phase envelope were conducted in the Simulations module. The stability of the simulation results is referenced in Qiao and Chen (2022).

3.2.4. One-dimensional burial-thermal modeling

The burial and thermal histories of three wells in the Shunbei oilfield were reconstructed using PetroMod software. Stratigraphic age and burial depth data were provided by SINOPEC Northwest Company (Urumqi). The formation denudation thickness was calculated based on the thickness ratio of adjacent strata and the change ratio of formation thickness using the connected well profile method outlined in Li et al. (2022a). The heat flow value reported by Li et al. (2022a) was initially adopted, then corrected and adjusted according to the equivalent vitrinite reflectance (calculated according to the bitumen reflectance).

3.2.5. Fluid inclusion analysis

Polished core samples from the Yijianfang and Yingshan Formations in the Shunbei oilfield were used to create inclusion plates about 0.08 mm thick. Microscopic fluid inclusion analysis was conducted using a Nikon-LV100 microscope equipped with dual channels for fluorescence. The homogenization temperature was measured on a LinkAM-THMSG600 cold and hot platform, which has a temperature range of −190 °C–600 °C and a temperature measurement error of ±0.1 °C. Oil inclusions were identified using a microfluorescence spectrometer (Maya-2000 pro, beam diameter 2 μm).

4. Results

4.1. Petroleum reservoir types and distribution

The Ordovician strata in the Shunbei oilfield contain a large number of light petroleum reservoirs. P-T phase diagrams show the presence of four distinct types of petroleum reservoirs within the No. 1 and No. 5 fault zones of the Shunbei oilfield: gas reservoirs (Fig. 3a), condensate reservoirs (Fig. 3b), volatile oil reservoirs (Fig. 3c), and light oil reservoirs (Fig. 3d). Combining this with the three-terminal diagram of fluid components, it is found that there are significant differences between the petroleum reservoir types in different strike-slip fault zones and between those in different sub-sections of the same strike-slip fault zone (Fig. 3e). The No. 5 fault zone is mainly distributed from south to north, with a GOR (cumulative produced gas-oil ratio) range of 64–279807 m^3/m^3 (Table 1). From south to north, the No. 5 fault zone consists of condensate reservoirs, gas reservoirs, condensate reservoirs, volatile oil reservoirs, and light oil reservoirs (Fig. 3 and Table 1). The No. 1 fault zone is mainly distributed in a NW direction, with a GOR range of 292–530 m^3/m^3, and predominantly contains volatile reservoirs (Fig. 3 and Table 1).

4.2. Bulk properties and carbon isotope compositions

Oil density in the study area varies from 0.766 to 0.840 g/cm^3, with an average of 0.807 g/cm^3. Viscosity ranges from 1.244 to 8.060 mm^2/s, with an average of 3.613 mm^2/s. The oils all have low wax (<10%), low sulfur (<0.5%) contents, and similar bulk properties (Table 1).

Analysis of carbon isotope composition shows the following values: Sat < Aro < Asp < Res. (Fig. 4). Saturated fractions, oil, aromatic fractions, resin, and asphaltenes have $\delta^{13}C$ values ranging from −32.9‰ to −29.1‰, −33.1‰ to −29.3‰, −31.7‰ to −28.4‰, −31.6‰ to −26.9‰, and −32.3‰ to −28.2‰, respectively (Table 1). The carbon isotope distributions in all the oils are basically the same (Fig. 4).

4.3. Saturated and aromatic hydrocarbon compositions

The oils from the Shunbei oilfield exhibit a complete series of *n*-alkanes in a single-peak distribution, with C_{11}–C_{13} as the predominant peak (Fig. 5, a1–e1). On the total ion chromatograms (TIC), the majority of the oils display slight baseline humps (Fig. 5, a1–e1). The abundance

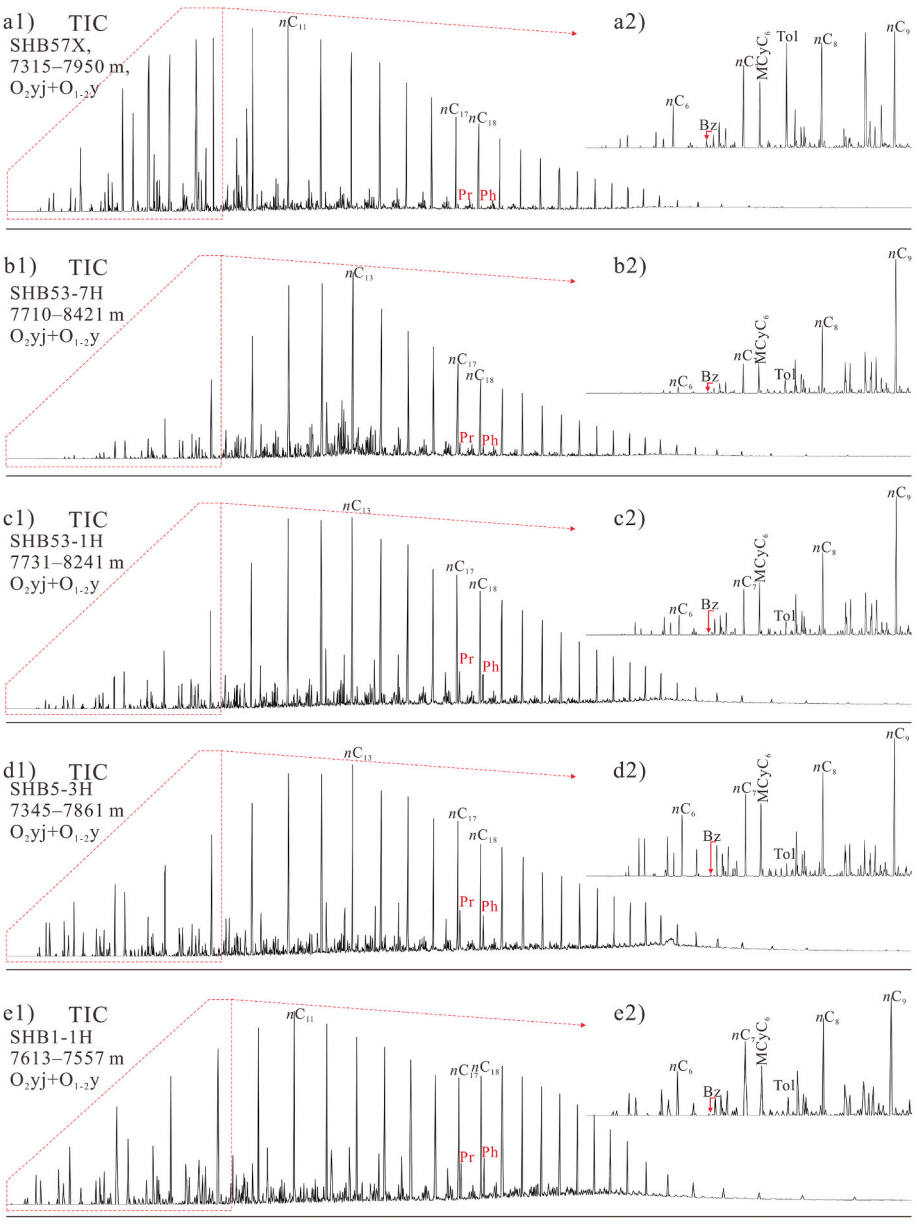

Fig. 5. Representative TIC of saturated hydrocarbon fraction (a1-e1) and light hydrocarbon gas chromatograms (a2-e2) of oils from the Shunbei oilfield.

of isoprenes was also notably lower compared to adjacent *n*-alkanes (Fig. 5, a1–e1).

The mass chromatograms of *m/z* 191 and *m/z* 217 indicate that the terpene and sterane biomarkers within the oil samples are generally well-preserved (Fig. 6, a1–e2). Only the well SHB57X retained a small amount of low-molecular-weight steranes and terpenes (Fig. 6, a1 and a2).

Mass chromatograms of *m/z* 177 reveal the whole series of 25-norhopanes (25-NHs) and nortricylic terpanes (17-NTs) in most of the Shunbei oils, except for samples from well SHB57X (Fig. 6, a3–e3). In addition, *m/z* 177 mass spectrometry revealed a higher abundance of 25-NHs and 17-NTs compounds in oils from the mid-north sub-sections of the No. 5 fault zone compared to the No. 1 fault zone (Fig. 6, b3–e3).

Abundant aromatic compounds were detected in the Shunbei oils (Fig. 7). However, the TIC of the aromatic hydrocarbons did not exhibit any obvious baseline humps (Fig. 7). GC-MS of the aromatic fractions detected >3-ring polycyclic aromatic hydrocarbons (PAHs) in addition to the more common ones such as naphthalene (Nap) and phenanthrene (Phe). Notably, coronene with up to 7-ring PAHs was detected (Fig. 7).

4.4. Light hydrocarbon and diamondoid compositions

In the study area, the light oils have a rich composition of light hydrocarbon parameters, with C_7 homologues being the most prevalent (Fig. 5, a2–e2). Gas chromatography revealed that the *n*-alkane content of the oil samples surpasses that of cycloalkanes and iso-alkanes (Fig. 5, a2–e2). Table 2 lists several light hydrocarbon parameters that are of particular significance for this study. The oil samples were also found to contain abundant diamondoid series compounds, with the total diamondoids ranging from 449.86 to 13762.56 μg/g and an average content of 2744.82 μg/g (Table 2).

4.5. Molecular and stable isotopic compositions

The drying coefficient of gas samples in the study area ranges from 0.52 to 0.99, with an average of 0.84 (Table 3). Most of the gas is wet

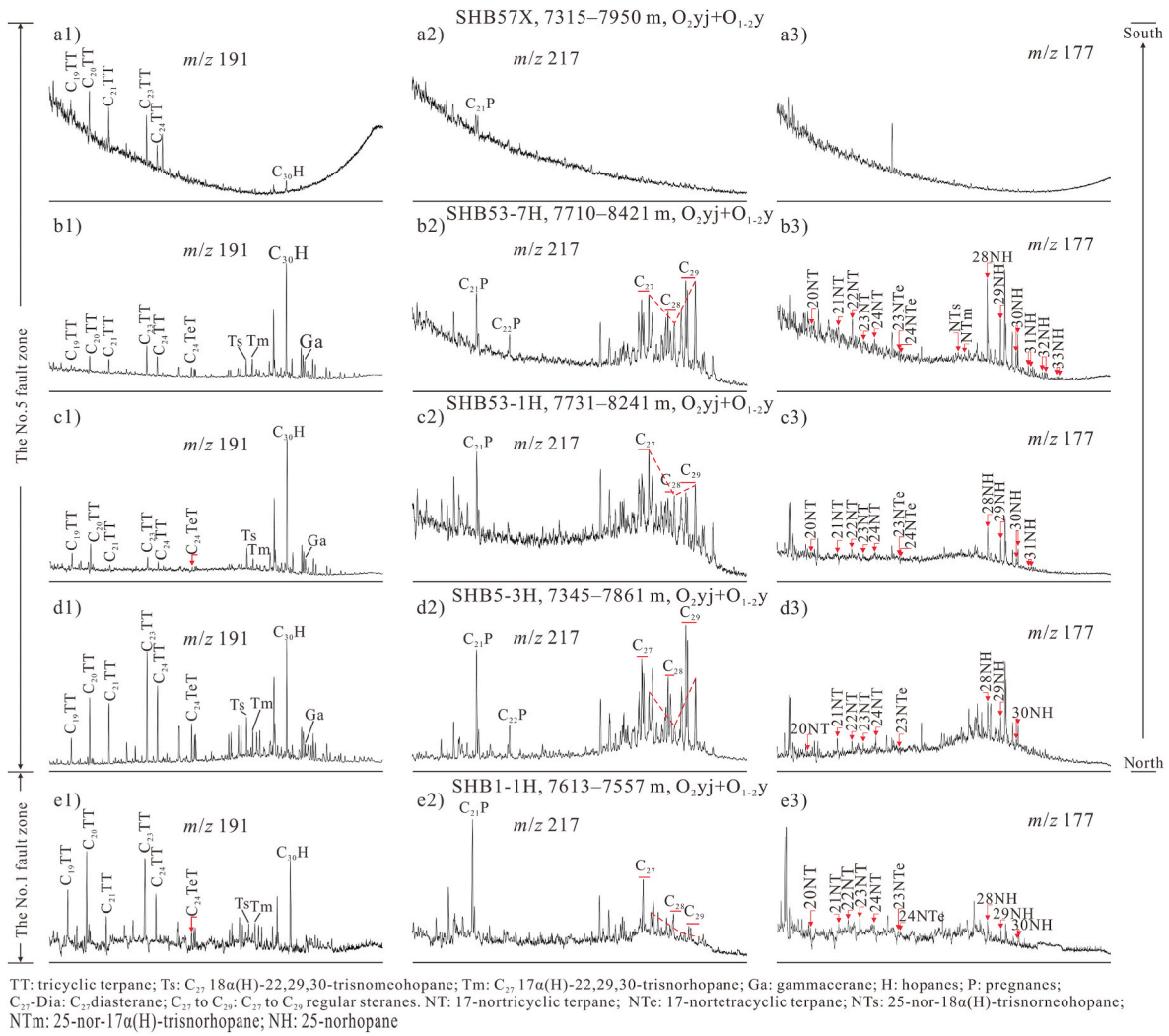

TT: tricyclic terpane; Ts: C_{27} 18α(H)-22,29,30-trisnomeohopane; Tm: C_{27} 17α(H)-22,29,30-trisnorhopane; Ga: gammacerane; H: hopanes; P: pregnanes; C_{27}-Dia: C_{27}diasterane; C_{27} to C_{29}: C_{27} to C_{29} regular steranes. NT: 17-nortricyclic terpane; NTe: 17-nortetracyclic terpane; NTs: 25-nor-18α(H)-trisnorneohopane; NTm: 25-nor-17α(H)-trisnorhopane; NH: 25-norhopane

Fig. 6. Mass chromatograms of *m/z* 191 (a1-e1), *m/z* 217 (a2-e2), and *m/z* 177 (a3-e3) for representative oils from the Shunbei oilfield.

(dryness<0.95), with only three wells in the south sub-section of the No. 5 fault zone being classified as dry gas (dryness>0.95) (Table 3).

The distributions of $\delta^{13}C_{CH4}$ and $\delta^{13}C_{CO2}$ range from −49.2‰ to −44.7‰ and −13.8‰–1.2‰, respectively, with an average of −47.16‰ and −3.08‰, falling within the ranges for thermogenic gas (Table 3).

4.6. Distribution of diabase intrusions

Seismic profiling revealed extensive igneous intrusions between T_7^0 and T_7^4. There was a strong difference in wave impedance between the igneous intrusions and the surrounding rock, resulting in a strong axis reflection nearly parallel to the sedimentary strata on the seismic profile (Fig. 8a). The lateral continuity of this reflection was restricted, forming saucer-shaped sills in space (Fig. 8a and b). A core retrieved from a depth of 6425–6430 m in well SHB1-3 was prepared for thin-section observation. Microscopic examination revealed a distinct diabase structure within the intrusive rock mass, confirming its classification as basic diabase (Fig. 8c and d). Seismic profile observations reveal significant diabase intrusions along the No. 1 fault zones and the south sub-sections of the No. 5 fault zones (Figs. 8 and 9a1, Fig. 9b1). However, no obvious diabase intrusions were observed in the mid-north sub-sections of the No. 5 fault zones (Fig. 9c1, Fig. 9d1).

5. Discussion

5.1. Origin of the deep petroleum

Normally, the carbon isotope values of oils from the same source fluctuate within a range of ±2‰–3‰ due to maturity (Peters and Moldowan, 1993). The distribution characteristics of carbon isotopes of oil in the study area are similar, with fluctuations of less than 3‰, indicating a common source for the oil samples (Fig. 4 and Table 1).

The Pr/nC_{17} and Ph/nC_{18} distributions for the oil samples are 0.05–0.39 and 0.04–0.49, respectively, with averages of 0.27 and 0.31 (Table 2). The distribution ranges for Pr/Ph and DBT/P are 0.75–1.67 and 0.12–1.82, with averages of 1.02 and 0.81 (Table 2). These values indicate that the oil in the area originated in a reducing environment with predominantly type II organic matter input (Fig. 10; Shanmugam, 1985; Hughes et al., 1995). Previous studies have shown that the petroleum in the Shunbei oilfield mostly comes from the source rocks of the $Є_1y$ (Ma et al., 2022; Bian et al., 2023).

5.2. Oil maturity

Petroleum is chemically complex, and assessing its maturity is crucial for characterizing its properties (Wilhelms and Larter, 2004; Justwan et al., 2006). Biomarkers, commonly present in organic matter, undergo side chain breaks, methyl rearrangement, isomerization, and

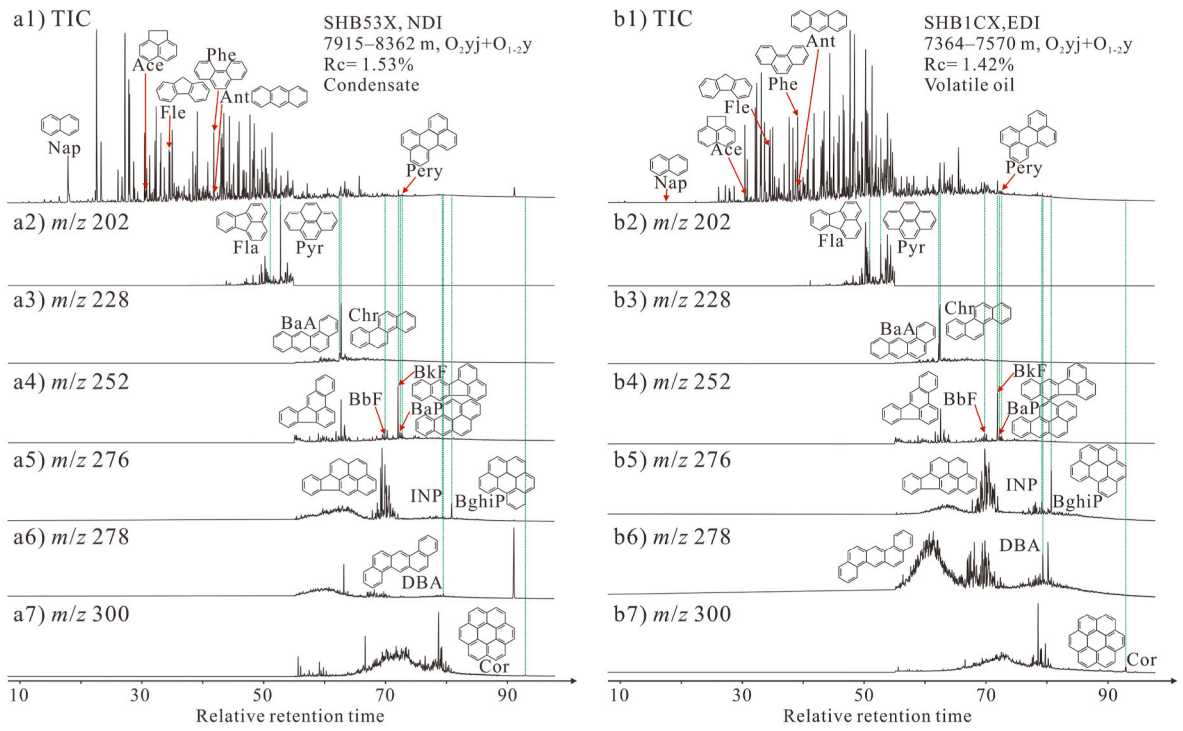

Nap: Naphthalene; Acy: Ace: Acenaphthylene; Acenaphthene; Fle: Fluorene; Phe: Phenanthrene; Ant: Anthracene; Fla: Fluoranthene; Pyr: Pyrene; BaA: Benz[a]anthracene; Chr: Chrysene; BbF: Benzo[b]fluoranthene; BkF: Benzo[k]fluoranthene; BaP: Benzo[a]pyrene; Pery: Perylene; INP: Indeno[1,2,3-cd]pyrene; BghiP: Benzo[g,h,i]perylene; DBA: Dibenz[a,h]anthracene; Cor: Coronene; MD: methyldiamantane; MDI: methyldiamantane index; MDI = 4-MD/(1-MD+3-MD+4-MD); Rc_{oil}: Rc_{oil}= 0.4389+ 0.0243MDI (Chen et al., 1996); EDI: Exist diabase intrusion; NDI: No diabase intrusion

Fig. 7. TIC of aromatic hydrocarbon fraction and mass chromatograms of polycyclic aromatic hydrocarbon (*m/z* 202+ *m/z* 228+ *m/z* 252+ *m/z* 276+ *m/z* 278+ *m/z* 300) for representative oils from the Shunbei oilfield. a) SHB53X; b) SHB1CX.

aromatization during thermal evolution. These transformations provide valuable insights into the degree of thermal evolution in organic matter and are widely employed in assessing oil maturity (Mackenzie et al., 1980; Radke et al., 1982; Alexander et al., 1983).

When oil reaches high maturity, there are reversals in most of the parameters used for evaluating the maturity of saturated and aromatic hydrocarbons (Seifert and Moldowan, 1978; Radke et al., 1982). Despite this, light hydrocarbons and diamantanes are present in abundance during the high maturity stage and are effective for assessing oil maturity (Thompson, 1983; Chen et al., 1996). The samples in this study exhibit high heptane and isoheptane values, indicating high maturity (Fig. 11a). In addition, the sample analyzed in Fig. 8a is derived from type I or type II organic matter. The diamantane parameters affirm overall high maturity (Fig. 11b). The calculated equivalent vitrinite reflectance (*Rc*; *Rc* = 0.4389 + 0.0243MDI) based on MDI ranged between 1.27% and 1.60% (Chen et al., 1996, Table 2). Specifically, the maturity sequence in fault zone No. 5 was: south sub-section > mid-sub-section > north sub-section, which correlates well with the petroleum phase distribution. However, the oil maturity in the west sub-section of the No. 1 fault zone is slightly higher than in the east sub-section.

5.3. Reservoir secondary alteration

5.3.1. Biodegradation and mixing

Biodegradation is a crucial secondary alteration in reservoirs, with significant economic implications for petroleum exploitation (Sun et al., 2005). Previous studies have suggested that bacteria struggle to survive at temperatures exceeding 88 °C, with only a limited population of thermophilic bacteria enduring at 102 °C (Stetter et al., 1993). Detecting biodegradation in ultra-deep oil therefore confirms the early filling of reservoirs.

A complete distribution of *n*-alkanes was found in the oil samples in the study area, as well as a relatively complete 25-NHs series, which was detected in all samples except those from well SHB57X (Fig. 6, a3–e3). Previous studies have suggested that the presence of the 25-NHs series indicates significant biodegradation in the reservoir (Volkman et al., 1983; Cai et al., 2007). However, during the biological decomposition of oils, *n*-alkanes are the first to be consumed (Peters and Moldowan, 1993). The coexistence of intact *n*-alkanes and 25-NHs in the sample suggests that early biodegraded oil was mixed with subsequently charged fresh oil (Wang et al., 2022). The absence of 25-NHs in the oils from well SHB57X could be explained in three ways. First, the reservoir may not have been formed at an early stage; second, oil in the early stage of reservoir formation may not have undergone biodegradation; and third, oil in the early stage of reservoir formation may have experienced biodegradation, but the biomarkers were destroyed by cracking.

5.3.2. Thermochemical sulfate reduction

Thermochemical sulfate reduction (TSR) in carbonate reservoirs can result in H_2S enrichment (Krouse et al., 1988). The gas in the study area has a relatively high H_2S content, likely influenced by TSR (Wang et al., 2021). Previous research has indicated that the K_1 value (K_1 = (2-MH+2,3-DMP)/(3-MH+2,4-DMP)) in oil unaffected by TSR typically hovers around 1.0. However, TSR activity can lead to an elevated K_1 value (Mango, 1997). As shown in Fig. 12a, the K_1 values for wells SHB53–2H and SHB57X significantly exceed 1, similar to the values found in samples known to have been impacted by TSR in the Tazhong. This indicates that the study samples may also have suffered a strong TSR effect. TSR involves hydrocarbons reacting with H_2S, forming various organic sulfur-containing compounds (e.g., thiolanes, thiols, alkylbenzothiophenes, and alkyl-2-thiaadamantanes) (Orr, 1974; Cai et al., 2016). Combining the K_1 value and the total concentration of dibenzothiophene series compounds (DBTs), it is found that the DBT

Table 2
Biomarker, light hydrocarbon, and diamondoid parameters of oils from the Shunbei oilfield.

Well	A	B	C	D	E	F	G	H	I	J	K	L	M	N	O	P	Q	R	S	T	U	V
											μg/g				%					%		
SHB57X	0.05	0.04	1.35	1.64	1.38	34.70	3.51	1.47	1.15	0.27	314.93	0.00	147.12	5379.31	74.11	47.35	1.59	86.41	78.21	51.72	19.20	29.08
SHB53–7H	0.12	0.11	1.21	1.82	1.05	29.48	2.89	0.69	1.77	0.26	424.39	5.82	409.73	13762.56	84.82	46.76	1.58	95.12	89.01	70.95	25.06	4.00
SHB53–2H	0.07	0.05	1.67	1.54	1.19	31.81	3.93	1.51	2.16	0.30	582.35	0.20	385.30	11649.88	80.51	47.94	1.60	94.81	88.63	44.38	19.30	36.32
SHB55X	0.21	0.21	1.10	1.04	1.10	34.73	2.69	0.73	1.19	0.18	704.92	2.93	187.22	3985.97	74.11	43.93	1.51	89.32	81.82	74.23	16.51	9.27
SHB53–1H	0.24	0.25	1.06	0.73	1.08	23.14	2.69	0.43	1.75	0.19	609.81	3.19	97.47	2410.99	72.91	45.47	1.54	79.48	69.62	75.23	18.09	6.68
SHB53X	0.29	0.34	0.99	0.47	1.07	29.42	2.20	0.63	0.91	0.14	695.67	4.61	71.11	1447.83	71.66	44.74	1.53	71.87	60.19	81.00	13.01	5.99
SHB5-10	0.29	0.35	0.94	0.45	1.02	27.12	2.18	0.23	0.99	0.13	625.48	5.03	40.56	924.16	71.23	43.24	1.49	50.69	33.91	84.05	12.77	3.18
SHB52A	0.36	0.39	1.02	1.53	1.03	35.03	2.51	0.27	1.75	–	842.95	–	–	–	–	–	–	–	–	–	–	–
SHB5-7	0.37	0.25	0.78	0.52	1.04	34.75	1.78	0.28	1.84	–	493.85	5.54	31.91	857.97	68.13	43.34	1.49	37.32	17.34	–	–	–
SHB5	0.36	0.26	0.84	1.02	1.03	34.68	1.74	0.18	1.76	–	547.55	14.12	38.33	296.14	67.81	43.54	1.50	47.82	30.36	–	–	–
SHB5–3H	0.33	0.36	1.02	0.34	1.02	26.70	1.50	0.18	1.05	0.15	602.54	17.09	38.01	653.03	72.89	44.70	1.53	47.38	29.81	79.97	14.45	5.58
SHB1–5H	0.27	0.40	0.78	0.35	1.01	38.33	2.22	0.35	1.63	–	437.88	0.00	33.86	1142.74	71.54	45.21	1.54	40.93	21.81	–	–	–
SHB1–4H	0.37	0.38	1.06	0.12	1.02	37.10	2.25	0.33	1.67	–	574.73	–	–	–	–	–	–	–	–	–	–	–
SHB1–23H	0.27	0.38	0.96	0.82	1.18	37.54	2.24	0.37	1.76	–	479.41	–	–	–	–	–	–	–	–	–	–	–
SHB1–1H	0.26	0.38	0.81	0.74	1.03	38.96	2.30	0.39	1.74	0.25	742.73	1.91	28.74	1049.04	72.79	41.72	1.45	30.41	8.76	69.92	23.48	6.60
SHB1–7H	0.32	0.36	1.15	0.44	1.04	34.01	2.29	0.37	1.72	–	483.16	1.54	31.54	1187.04	73.15	47.15	1.59	36.59	16.43	–	–	–
SHB1–6H	0.27	0.41	0.82	0.39	1.04	36.83	2.33	0.38	1.72	–	760.04	–	–	–	–	–	–	–	–	–	–	–
SHB1–8H	0.28	0.34	0.91	0.46	1.05	34.64	2.39	0.36	1.79	–	692.76	–	–	–	–	–	–	–	–	–	–	–
SHB1-9	0.25	0.36	0.82	1.21	1.04	32.82	2.24	0.27	1.30	0.24	481.48	2.75	30.68	1112.36	72.62	40.96	1.44	34.81	14.22	68.41	21.12	10.47
SHB1CX	0.36	0.35	1.07	1.29	1.04	33.15	2.86	0.18	2.13	0.22	453.07	3.12	30.09	1118.56	74.72	40.21	1.42	33.53	12.64	69.44	19.29	11.27
SHB1	0.32	0.35	1.41	0.64	0.97	40.71	2.02	0.22	1.63	–	608.09	14.50	22.42	746.82	68.76	34.25	1.27	10.79	0.00	–	–	–
SHB1–3CH	0.39	0.49	0.96	0.45	1.05	34.79	2.44	0.36	1.77	0.23	504.90	2.54	29.79	1232.56	73.62	40.32	1.42	32.86	11.81	72.43	21.07	6.50
SHBP1	0.27	0.41	0.75	0.56	0.98	34.81	1.94	0.25	1.41	0.15	273.78	7.35	16.92	449.86	67.26	35.65	1.31	0.00	0.00	80.74	14.42	4.83

A: Pr/nC_{17}; B: Ph/nC_{18}; C: Pr/Ph; D: DBT/P; E: K_1, K_1 = (2-MH+2,3-DMP)/(3-MH +2,4-DMP) (Mango, 1997); F: Heptane value, Heptane Value = (nC_7 × 100)/(CH + 2-MH + 2,3-DMP + 1,1-DMCP + 3-MH + 1c3-DMCP + 1t3-DMCP + 1t2-DMCP + nC_7 + MCH); G: Isoheptane value, Isoheptane Value = (2 + 3)-MH/(1c3 + 1t3 + 1t2)-DMCP; H: B, B = Tol/nC_7; I: F, F = nC_7/MCH; J: Indeno[1,2,3-cd]pyrene/(Indeno[1,2,3-cd]pyrene + Benzo[g,h,i]perylene); K: the concentration of total dibenzothiophene series compounds (DBTs); L: the concentration of ααα(20 R)-C_{29} sterane; M: the concentration of 3-+4- Methyldiamantane; N: the concentration of total diamondoids; O: MAI, MAI = 1-MA/(1-MA+2-MA); P: MDI, MDI = 4-MD/(1-MD+3-MD+4-MD); Q: Rc, Rc (%) = 0.4389 + 0.0243MDI (Chen et al., 1996); R: EOC1, EOC1 = [1 − C_0/C_c] × 100 (Dahl et al., 1999); S: EOC2, EOC2 = 1.2402 × EOC1 − 28.952 (Peng et al., 2022); T: Benzo[g,h,i]perylene; U: Indeno[1,2,3-cd]pyrene; V: Coronene; "–" = no data or not determined.

Table 3
Molecular and stable isotopic compositions of gases from the Shunbei oilfield.

Well	Dryness	Molecular Composition, mol %										$\delta^{13}C_{PDB}$, ‰								Pco_2
		N_2	CO_2	C_1	C_2	C_3	iC_4	nC_4	iC_5	nC_5	C_6^+	C_1	C_2	C_3	iC_4	nC_4	iC_5	nC_5	CO_2	
SHB57X	0.98	2.42	1.86	94.18	1.29	0.16	0.04	0.02	0.01	0.01	0.01	–	–	–	–	–	–	–	–	82.21
SHB53–7H	0.99	1	6.95	91.27	0.65	0.08	0	0	0	0	0.048	−45.6	−28.2	−27.2	−27.3	−27.4	–	–	−8.8	471.28
SHB53–2H	0.96	6.98	2.97	86.79	2.15	0.49	0.17	0.22	0.01	0.12	0.11	−48.2	−27.5	−24.5	−25.6	−24.6	−26	−26.6	−4.6	174.90
SHB55X	0.93	0.87	19.05	74.43	3.57	1.03	0.24	0.48	0.13	0.17	0.04	−47.3	−32.1	−29.3	−31.2	−29.2	–	–	−4.1	1459.61
SHB53–1H	0.91	0.62	3.81	86.78	5.44	1.88	0.37	0.73	0.15	0.19	0.04	−48.4	−32.8	−30.4	−31	−29.9	–	–	−9.6	165.24
SHB53X	0.84	4.96	6.49	74.51	7.9	3.08	0.68	1.44	0.38	0.5	0.06	−47.7	−33.4	−31.7	−31.4	−30.4	−30.3	−29.8	−13.8	218.32
SHB5–15H	0.87	2.52	2.15	83.25	8.15	2.73	0.37	0.62	0.09	0	0.12	−47.6	−33.3	−30.6	−30.8	−29.5	–	–	−0.5	110.32
SHB5-10	0.88	4.17	2.07	82.07	8.35	2.41	0.27	0.44	0.06	0.16	0.01	−47.5	−33.5	−30.7	−31.8	−29.4	–	–	−1.1	128.01
SHB52A	0.77	5.89	19.92	56.95	9.76	4.4	0.82	1.46	0.33	0.37	0.1	−47.3	−33.3	−30.7	−31.7	−29.3	−29.5	−27.8	−2.3	1728.26
SHB5-7	0.84	3.81	1.65	79.88	9.31	3.48	0.47	0.84	0.11	0.45	0.01	−47.8	−33.6	−30.9	−31.1	−29.7	−29.6	−29.1	1.2	111.38
SHB51X	0.86	4.84	1.51	80.33	9.53	2.87	0.31	0.54	0.06	0	0.01	−48.2	−34	−31.2	−31.1	−29.6	–	–	−1.1	79.37
SHB5	0.63	5.84	8.06	54.48	17.97	9.43	1.09	2.15	0.46	0.36	0.16	−48.7	−39.3	−35.6	−34.6	−33.4	–	–	−3.7	692.11
SHB5–11H	0.58	11.97	2.25	49.18	15.73	10.85	2.06	4.73	1.21	1.58	0.46	−49.2	−38.6	−34.1	−33.7	−32.3	−31.6	−31.9	−2.5	125.35
SHB1–5H	0.87	3.81	2.62	81.68	6.6	2.92	0.65	1.05	0.28	0.3	0.09	–	–	–	–	–	–	–	–	100.03
SHB1–4H	0.84	2.2	2.32	80.35	9.05	3.98	0.7	1.01	0.18	0.2	0.01	−47	−33.8	−31.6	−35.2	−29.4	−30.8	−28.5	0.5	151.66
SHB1–23H	0.85	2.57	16.61	68.83	7.57	2.58	0.39	0.92	0.34	0.18	0.02	−48.1	−34.8	−32.3	−32.9	−32	−31.3	−31.7	−1.6	1127.49
SHB1–1H	0.9	3.63	2.29	84.24	5.82	2.22	0.48	0.83	0.21	0.22	0.05	−46.4	−36.1	−36	−39.4	−35	–	–	–	173.58
Well	Dryness	Molecular Composition, mol %										$\delta^{13}C_{PDB}$, ‰								Pco_2
		N_2	CO_2	C_1	C_2	C_3	iC_4	nC_4	iC_5	nC_5	C_6^+	C_1	C_2	C_3	iC_4	nC_4	iC_5	nC_5	CO_2	
SHB1–7H	0.88	3.69	2.78	82.37	6.89	2.75	0.49	0.71	0.14	0.14	0.03	–	–	–	–	–	–	–	–	98.16
SHB1–6H	0.86	2.63	2.67	81.06	7.31	3.49	0.73	1.27	0.42	0.39	0.02	–	–	–	–	–	–	–	–	155.47
SHB1–8H	0.79	4.83	2.68	72.5	8.75	5.43	1.32	2.42	0.75	0.83	0.5	−47.2	−33.8	−31.2	−31.9	−30.7	–	–	−1.4	151.55
SHB1-9	0.88	4.2	2.3	81.99	6.18	3.53	0.65	0.87	0.14	0.12	0.02	−46.6	−34.2	−31.9	−31.9	−31.2	–	–	−2.1	179.45
SHB1CX	0.87	3.68	2.45	81.5	6.96	3.12	0.67	1.02	0.26	0.27	0.06	−46	−34.4	−32.1	−32.4	−31.4	–	–	−2.8	159.20
SHB1	0.89	3.32	2.4	83.41	6.6	2.62	0.51	0.75	0.17	0.17	0.04	−44.7	−33.1	−30.8	−31.3	−29.8	−30	−30.2	–	179.40
SHB1–3CH	0.88	3.11	2.41	82.7	6.76	2.97	0.57	0.9	0.23	0.23	0.12	−44.7	−33.3	−30.8	−34.2	−29	−31.6	−28.2	0.1	206.51
SHBP1	0.52	0.65	31.64	34.98	15.14	10.06	1.99	3.52	0.89	0.86	0.27	−46.1	−35.5	−33.1	−33.9	−32	–	–	−0.4	2040.46

"–": no data or not determined; Pco_2: partial pressures of CO_2, $Pco_2 = CO_2$ mol% × reservoir pressure.

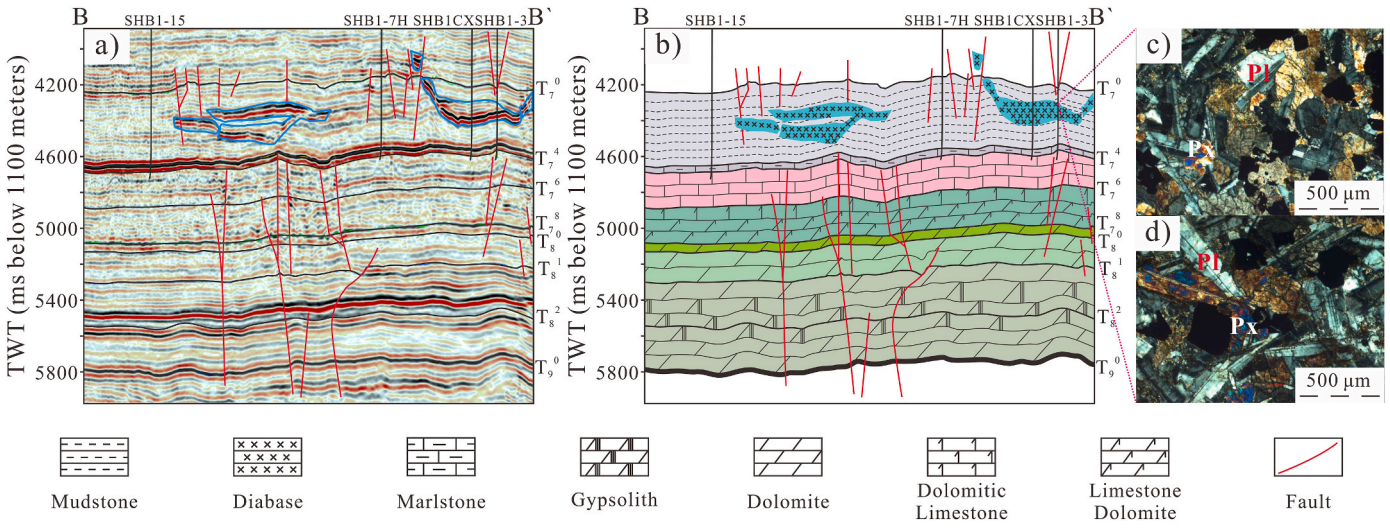

Fig. 8. Cross the No. 1 fault zone seismic section (a), the relevant geological schematic section (b),microscopic observation of the core at 6425–6430 m in well SHB1-3 (c and d).

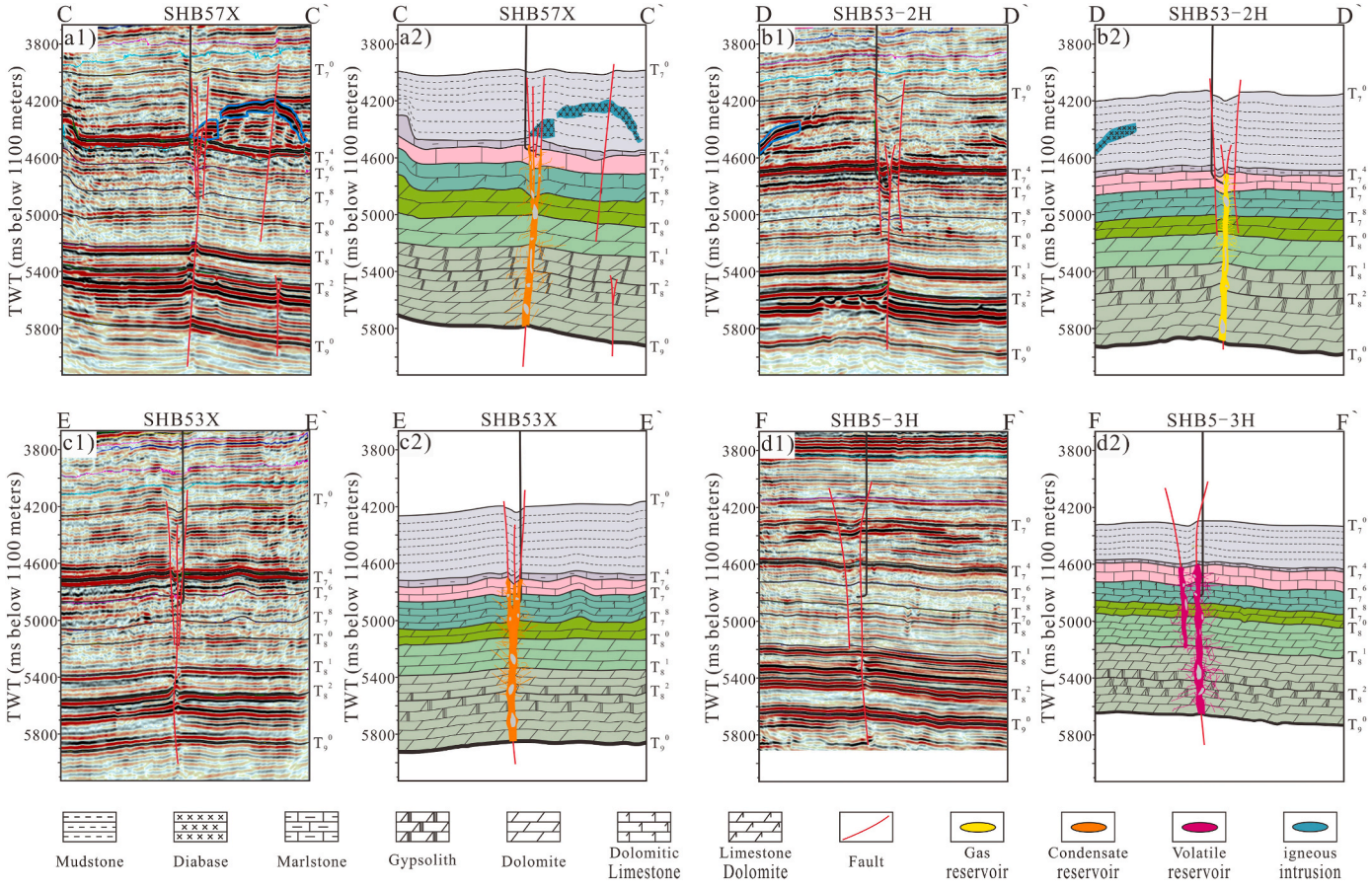

Fig. 9. Cross-well seismic section and relevant geological schematic section. SHB57X (a1 and a2); SHB53–2H (b1 and b2); SHB53X (c1 and c2); SHB5–3H (d1 and d2).

concentration in the oils of wells SHB53–2H and SHB57X is markedly lower than that of the oils subjected to TSR in the Tazhong area (Fig. 12b). Furthermore, the absence of salt-rock layers in the Ordovician strata suggests that conditions were unsuitable for TSR. Favorable locations for TSR reactions include the underlying Cambrian Awatage Formation and the Shayilike Formation, both of which have salt-rock layers, which suggests that TSR likely occurred in the underlying Cambrian reservoir. High proportions of H_2S and (2-MH+2, 3-DMP)/(3-MH+2,4-DMP) are associated with late gas filling into Ordovician reservoirs. Due to the high molecular weight of DBTs and the limited carrying capacity of the late-charged natural gas, DBTs did not accumulate significantly.

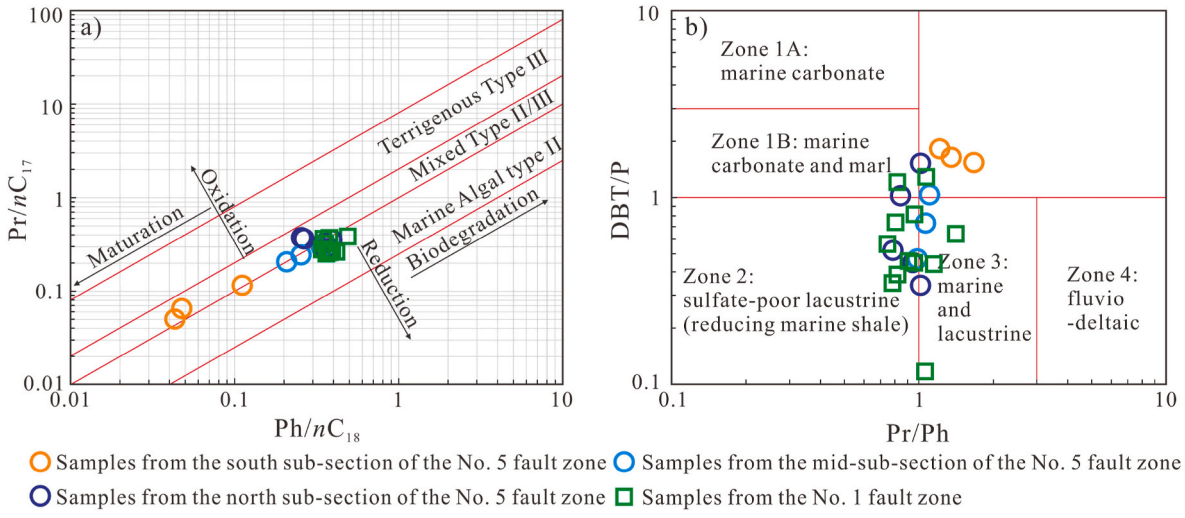

Fig. 10. Cross-plots identify sedimentary environments. a) phytane (Ph)/*n*-C_{18} versus pristane (Pr)/*n*-C_{17} (refer to Shanmugam, 1985); b) pristane (Pr)/phytane (Ph) versus dibenzothiophene (DBT)/dibenzothiophene (P) (refer to Hughes et al., 1995).

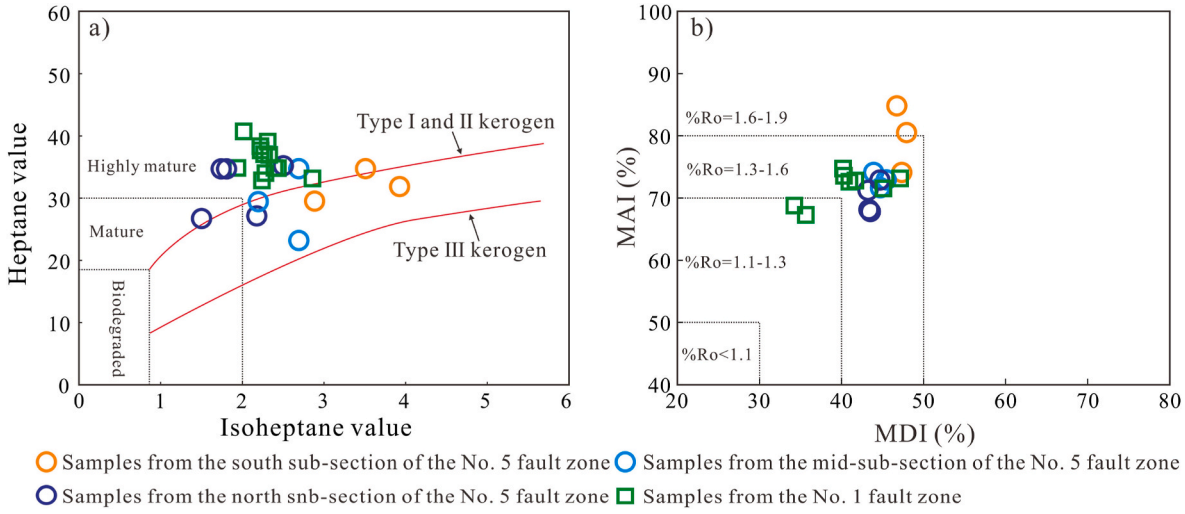

Fig. 11. Light hydrocarbon and diamondoids parameters identify the maturity of oils from the Shunbei oilfield. a) heptane value versus isoheptane value (modified after Thompson, 1983); b) MAI versus MDI (refer to Chen et al., 1996).

5.3.3. *Evaporative fractionation*

Evaporative fractionation is another significant secondary alteration in petroleum reservoirs, which plays a pivotal role in the formation of many light petroleum reservoirs (Mehay et al., 2021; Qiao et al., 2022). The logarithmic distribution of molar concentrations of *n*-alkanes reveals varying degrees of loss of low-to medium-molecular-weight *n*-alkanes from the oil in the study area (Fig. 13, a–f; Kissin, 1987). This signifies evaporative fractionation in the reservoirs. B–F diagram identification shows that the order of the intensity of evaporative fractionation in the study area is: south sub-sections of the No. 5 fault zone > mid-sub-sections of the No. 5 fault zone > No. 1 fault zone > north sub-sections of the No. 5 fault zone (Fig. 13g and h; Thompson, 1987). The southern sub-sections of the No. 5 fault zone experienced the most pronounced evaporative fractionation, pointing to robust late-stage natural gas filling. This explains why the petroleum phase is gas and condensate gas reservoirs, although the reservoir temperature distribution of the south sub-sections of the No. 5 fault zone is 157.67°C–170.63 °C (Fig. 3 and Table 1). Evaporative fractionation has significantly influenced the phase distribution of petroleum in the study area, playing a crucial role in the petroleum accumulation process.

5.3.4. *Thermal alteration and cracking*

Magmatic activity has occurred frequently in the Shunbei oilfield since the Paleozoic, with the Permian magmatic activity (290 Ma–259 Ma) standing out as the most intense and extensive episode (Xu et al., 2015). Faults that were reactivated during the Permian period served as conduits for magma upwelling (Ning et al., 2022). When the magma reached the Sangtamu Formation (O_3s), it encountered a substantial series of mudstone layers, resulting in lateral flows that formed igneous intrusions (Martín-Martín et al., 2015) (Figs. 8 and 9).

The regional thermal anomalies resulting from magmatic activity created favorable conditions for hydrothermal activity (Li et al., 2022b). U–Pb dating of calcite and the analysis of rare-earth elements in calcite veins in Ordovician reservoirs in the Shunbei oilfield indicated that a phase of hydrothermal activity occurred in the deep basin during the Permian period (Li et al., 2023). XU et al. (2022) clarified that the oil in the study area was affected by different degrees of thermal alteration through the transformation of PAHs.

Hydrothermal activity typically yields significant amounts of unresolved complex mixtures and >5-ring PAHs (Yamanaka et al., 2000; McCollom and Seewald, 2006; Xu et al., 2024). The TIC of saturated and aromatic hydrocarbons in the oils from Shunbei oilfield does not show

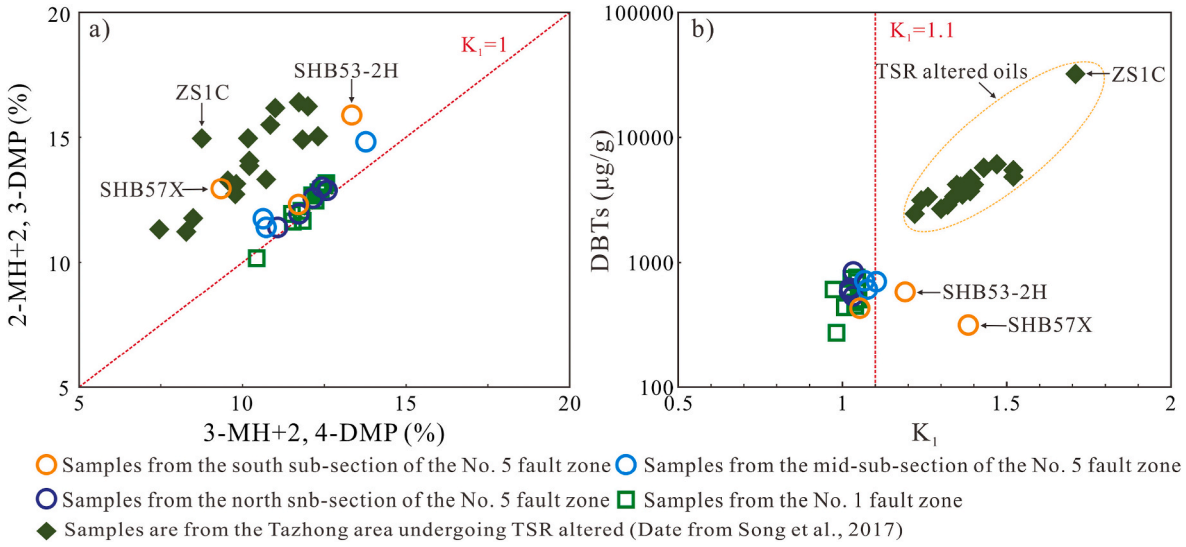

Fig. 12. Cross-plots identify the thermochemical sulfate reduction of oils from the Shunbei oilfield. a) 3-MH+2,4-DMP (%) versus 2-MH+2,3-DMP (%); b) K_1 versus concentrations of DBTs (Data on the Tazhong are from Song et al., 2017).

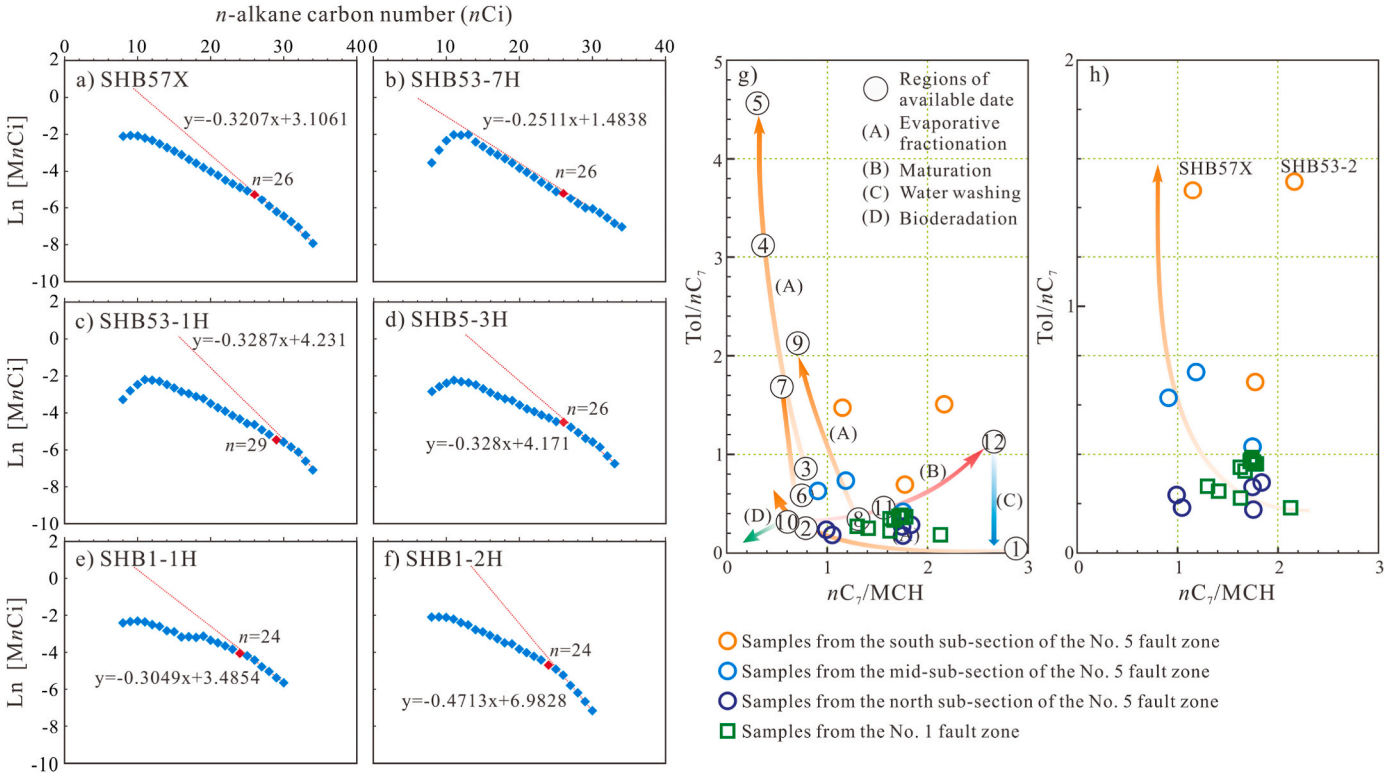

Fig. 13. Cross-plots indicating the differential evaporation fractionation of oils from the Shunbei oilfield. Log of mole concentration of C_5–C_{35} *n*-alkanes versus carbon numbers (a–f), Tol/nC_7 versus nC_7/MCH (g and h) (refer to Thompson, 1987).

an obvious baseline hump on the chromatograms (Figs. 5 and 7). Nonetheless, the aromatic hydrocarbons contain a series of 2–7 ring PAHs (Fig. 7). Analysis of diabase intrusion distribution and the relative percentage contents of 6–7 ring PAHs indicates higher levels of Indeno [1,2,3-cd]pyrene (INP) and coronene (Cor) in oils from the reservoirs with diabase intrusions (Fig. 14). The ratio of Indeno[1,2,3-cd]pyrene/(Indeno[1,2,3-cd]pyrene + Benzo[g,h,i]perylene) is greater than 0.2 in the oils from reservoirs with diabase intrusions (Table 2). This indicates that its presence is a result of oil combustion (Yunker et al., 2002). Microscopic observations also show substantial deposits of black solid bitumen distributed within the edges and suture lines of dissolved filled calcite (Fig. 15). Taken together, these findings suggest that oil in the early reservoir formation underwent thermal alteration due to hydrothermal activities.

Hydrothermal fluid upwelled along the magma pathway and infiltrated the reservoir, destroying the petroleum. Due to the surrounding rock's thermal conductivity, oil near the magma pathway underwent greater thermal alteration compared to regions farther away (Davies and Smith, 2006). The pronounced impact of hydrothermal activity is evident in reduced biomarker concentrations of saturated hydrocarbons,

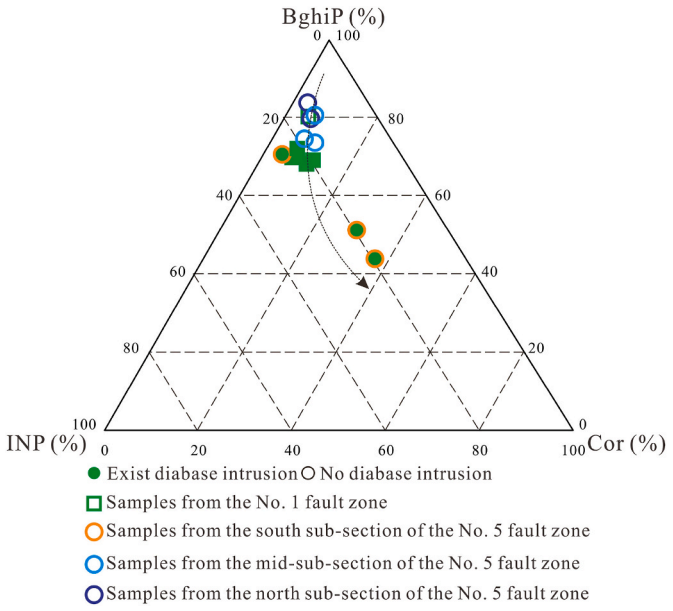

Fig. 14. Ternary diagrams showing the relative abundance of Benzo[g,h,i] perylene (BghiP), Indeno[1,2,3-cd]pyrene (INP) and Coronene (Cor) for representative oils from the Shunbei oilfield.

mass spectrometry baseline drift, and higher levels of INP and Cor (Fig. 6; Fig. 7; Fig. 14).

Previous studies have proposed that carbon isotopes of *n*-alkanes effectively record organic matter source information (Cai et al., 2015). The variation range influenced by maturity is between 2.0‰ and 3.0‰ (Clayton and Bjorøy, 1994). The distribution characteristics of carbon isotopes of *n*-alkanes in the study area are generally consistent, with only well SHB57X exhibiting heavier isotope characteristics (Fig. 16). This suggests a common source for the oils, which potentially originated from lower Cambrian source rocks (Cai et al., 2015; Wang et al., 2021).

Previous research indicates a substantial increase in carbon isotopes of *n*-alkanes in oils sourced from Cambrian rocks following TSR and thermal alteration (Cai et al., 2015; Z. Chen et al., 2022). The carbon isotope distribution of *n*-alkanes in well SHB57X resembles those of well ZS1C (which was affected by TSR) and well TD2 (which was affected by thermal alteration) (Fig. 16; Li et al., 2010a, 2010b; Cai et al., 2015; Huang et al., 2015). The study shows no obvious TSR effects in the SHB57X oil, but there is obvious evidence of thermal alteration. The SHB57X oil likely underwent significant thermal alteration, resulting in heavier isotopes due to thermal fractionation (Fig. 16) (Table 4).

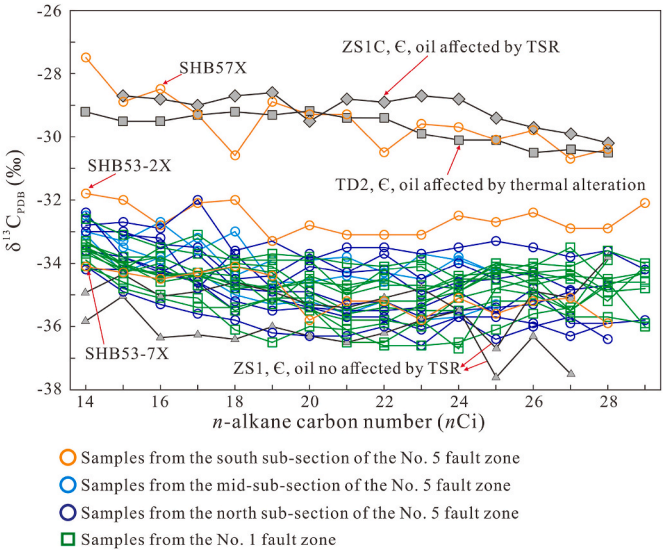

Fig. 16. Cross-plots of carbon number and carbon isotope compositions of *n*-alkane patterns of oils from the Shunbei oilfield. Comparative data for ZS1 oil is from Cai et al. (2015), ZS1C oil data is from Li et al. (2015), and TD2 oil data is from Li et al. (2010a).

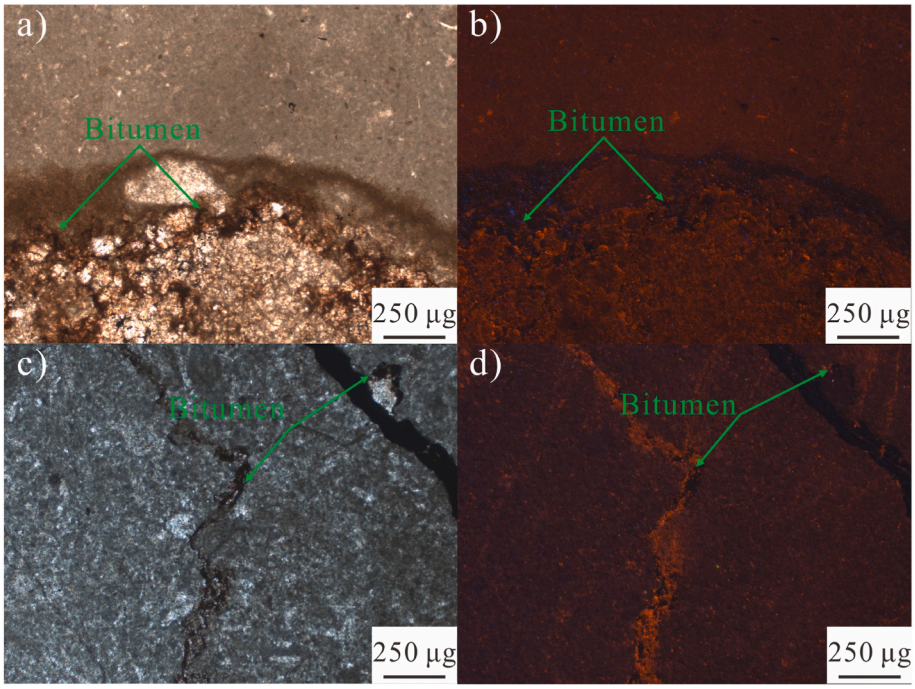

Fig. 15. Photomicrographs showing the petrological observations of the rocks in the Qiaerbake (O_3q) and Yijianfang (O_2yj) reservoirs of the wells SHB1–7H and SHB1–3CH. a) and c) are the transmitted light; b) and d) are the cold cathodoluminescence; a) and b): SHB1–7H, 7349.06 m, O_3q; c) and d): SHB1-3, 7287.00 m, O_2yj.

Table 4
The carbon isotopic compositions of *n*-alkanes of oils from the Shunbei oilfield.

Well	$\delta^{13}C_{PDB}$, ‰															
	C_{14}	C_{15}	C_{16}	C_{17}	C_{18}	C_{19}	C_{20}	C_{21}	C_{22}	C_{23}	C_{24}	C_{25}	C_{26}	C_{27}	C_{28}	C_{29}
SHB57X	−27.5	−28.9	−28.5	−29.3	−30.6	−28.9	−29.3	−29.3	−30.5	−29.6	−29.7	−30.1	−29.8	−30.7	−30.4	–
SHB53–7H	−34.1	−34.3	−34.5	−34.3	−34.1	−34.4	−35.8	−35.2	−35.2	−35.8	−35.1	−35.6	−35.2	−35.1	−35.9	–
SHB53–2H	−31.8	−32.0	−32.8	−32.1	−32.0	−33.3	−32.8	−33.1	−33.1	−33.1	−32.5	−32.7	−32.4	−32.9	−32.9	−32.1
SHB55X	−32.5	−33.5	−33.9	−33.2	−34.4	−33.9	−33.9	−33.8	−34.3	−34.5	−33.8	−34.3	–	–	–	–
SHB53–1H	−33.0	−33.3	−32.7	−33.6	−33.0	−34.6	−34.6	−34.4	−34.6	−33.7	−33.9	−34.3	–	–	–	–
SHB53X	−33.1	−34.3	−33.8	−34.3	−35.0	−35.3	−35.2	−35.6	−35.2	−35.8	−35.7	−35.3	–	–	–	–
SHB5-6	−33.6	−33.8	−34.3	−33.7	−34.8	−34.9	−34.9	−35.3	−35.2	−35.7	−35.5	−35.4	−35.3	−34.9	–	–
SHB52A	−32.8	−32.7	−32.9	−32.0	−33.7	−34.8	−34.1	−34.3	−33.7	−34.5	−34.0	−34.5	–	–	–	–
SHB501	−33.0	−33.0	−33.4	−33.5	−34.5	−34.4	−33.7	−34.3	−34.2	−35.0	−34.6	−34.5	−34.3	−34.9	−34.7	–
SHB5-1X	−32.6	−33.1	−33.2	−34.8	−33.6	−33.3	−33.9	−33.5	−33.5	−33.7	−33.5	−33.3	−33.5	−33.8	−33.6	−34.2
SHB5-2	−34.1	−34.9	−35.3	−35.6	−35.8	−36.2	−36.3	−36.3	−36.0	−36.6	−35.7	−36.4	−36.0	−35.7	−36.4	–
SHB5	−34.2	−34.2	−34.3	−34.6	−35.5	−35.1	−35.4	−35.5	−35.5	−35.4	−34.9	−35.6	−34.8	−35.9	−35.9	–
SHB5-4	−32.4	−33.8	−34.2	−34.6	−35.2	−35.5	−35.4	−35.7	−35.7	−36.1	−35.7	−35.7	−35.9	−36.3	−35.9	−35.8
SHB1–2H	−33.4	−33.8	−33.8	−34.3	−34.0	−34.1	−34.9	−35.5	−35.2	−35.2	−34.9	−34.3	−34.0	−34.1	−33.6	−34.0
SHB1–5H	−33.3	−34.1	−34.4	−34.4	−34.8	−34.7	−35.4	−36.1	−35.9	−35.3	−34.7	−34.1	−34.7	−34.4	−34.5	−34.3
SHB1–4H	−33.5	−34.2	−34.3	−34.4	−34.6	−34.8	−34.5	−35.0	−34.7	−34.7	−34.8	−34.0	−34.3	−34.5	−34.9	−34.8
SHB1–1H	−34.1	−34.6	−35.0	−35.1	−36.1	−36.5	−36.0	−36.1	−36.6	−36.6	−36.5	−36.1	−35.6	−35.4	–	–
SHB1–7H	−33.3	−34.0	−33.8	−34.3	−34.7	−34.8	−34.6	−34.7	−34.5	−34.9	−34.5	−34.0	−34.1	−33.5	−34.6	−34.6
SHB1–6H	−33.6	−34.0	−34.6	−34.4	−34.1	−34.3	−35.4	−36.5	−36.5	−35.8	−36.7	−34.8	−34.5	−34.4	−35.2	−34.1
SHB1–10H	−33.6	−34.3	−34.0	−34.7	−35.5	−35.1	−35.5	−35.8	−35.8	−36.0	−35.1	−34.8	−35.0	−35.5	−34.6	−36.0
SHB1CX	−33.9	−34.8	−35.1	−35.4	−35.4	−35.1	−35.1	−35.6	−35.4	−35.5	−35.5	−35.2	−35.2	−35.7	−35.7	−35.9
SHB1	−33.7	−34.2	−33.5	−33.7	−33.9	−33.9	−33.9	−35.0	−34.2	−34.1	−34.9	−34.2	−34.4	−35.5	−33.9	–
SHB1–3CH	−33.5	−34.0	−34.4	−34.3	−34.4	−35.3	−34.4	−34.8	−34.5	−34.9	−34.4	−34.3	−34.3	−34.2	−34.9	–
SHBP1	−32.6	−33.1	−33.5	−33.1	−33.9	−33.7	−33.8	−34.0	−34.1	−33.9	−34.5	−34.5	−34.8	−35.5	−34.7	−34.3

"–": no data or not determined.

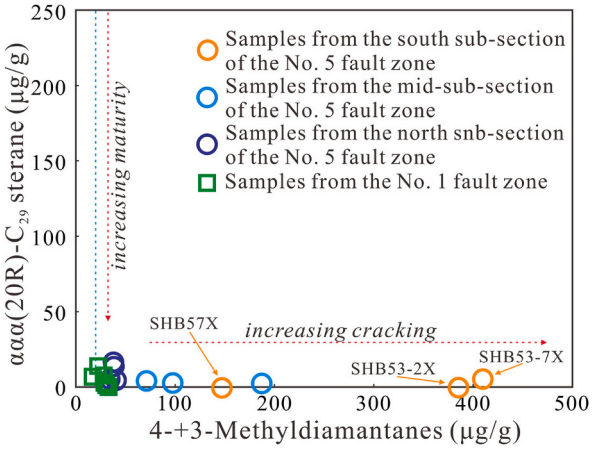

Fig. 17. Cross-plots of ααα(20 R)-C_{29}sterane and 3-+4-methyldiamantane concentrations of oils from the Shunbei oilfield (Dahl et al., 1999).

Fig. 17 shows the significant variations in the extent of oil-gas conversion across the study area. The overall sequence of oil-gas conversion was as follows: south sub-sections of the No. 5 fault zone > mid-sub-sections of the No. 5 fault zone > north sub-sections of the No. 5 fault zone > No. 1 fault zone. Dahl et al. (1999) quantified the extent of oil-gas conversion (EOC1) using the formula EOC1 = [1 − C_0/C_c] × 100, based on the concentrations of 4-+3-methyldiamantane.

Peng et al. (2022) concluded from simulation experiments that EOC1 is high when 1.2%< Rc <3.0%, and the formula EOG2 = 1.2402 × EOC1-28.952 was employed to correct non-TSR altered oil. The calculation reveals that oil-gas conversion in the No. 1 fault zone and northern sub-sections of the No. 5 fault zone ranges from 0 to 33.91%, indicating the initial stage of oil cracking (Table 2). The extent of oil-gas conversion was higher in the mid-south sub-sections of the No. 5 fault zone, ranging from 69.62% to 89.01% (Table 2). Interestingly, despite nearly complete cracking of the SHB57X biomarker, the oil-gas conversion in that well was not the highest (Table 2 and Fig. 17), suggesting that Permian hydrothermal activity is not the main factor controlling oil-gas conversion but that it has an important influence on the preservation of saturated hydrocarbons.

5.4. Origin of natural gas

The molecular and stable isotopic compositions of natural gas effectively capture its source and genesis information (Schoell, 1983; Dai, 1992). The cross plot of $\delta^{13}C_1$ and $C_1/(C_2+C_3)$ reveals that the natural gas in the study area is predominantly thermogenic (Fig. 18a; Milkov and Etiope, 2018).

Previous studies have established an average bulk rock $\delta^{13}C$ value of +1.8‰ for the Ordovician limestone in the Tarim Basin (Cai et al., 2001). The $\delta^{13}C$ values for CO_2 derived from carbonate decomposition should be similar to limestone values. The high $\delta^{13}C$ values for CO_2 in the study area may be due to carbonate dissolution (Table 3). However, combining the analyses of reservoir temperature, CO_2 molar volumes, and partial pressures of CO_2 (Pco_2, calculated as CO_2 mol% × reservoir pressure), shows that the CO_2 molar volumes and Pco_2 do not increase with increasing temperature (Tables 1 and 3). This indicates that limestone dissolution is not a major factor in the increase of molar volumes and $\delta^{13}C$ values for CO_2 in the study area (Coudrain-Ribstein et al., 1998; Hutcheon and Abercrombie, 1990; Cai et al., 2001).

It was found in this study that much of the oil has undergone significant biodegradation. Petroleum can generate secondary microbial gas (SMG) via biodegradation in reducing environments (Head et al., 2003). Due to significant carbon isotope fractionation during CO_2/H_2 methanogenesis, the residual $\delta^{13}C_{CO2}$ value can reach +15‰–+20‰ (Jones et al., 2008). Consequently, reservoirs with an SMG mixture also exhibit higher molar volumes and $\delta^{13}C$ values for CO_2 (Milkov, 2011; Wang et al., 2022). Combined analysis of $\delta^{13}C_{CH4}$, $\delta^{13}Cco_2$, and CO_2 molar volumes indicates mixing of SMG in the No. 1 fault zone and the north sub-sections of the No. 5 fault zone (Fig. 18b and c). Additionally, when combined with the analysis of the mixing of SMG in the Tahe oilfield in the north of the study area, it was found that the proportion of SMG increased from south to north (Wang et al., 2022, Fig. 18b and c). However, in general, the study area is still dominated by thermogenic gases. The oil in the No. 1 fault zone and the north sub-sections of the No. 5 fault zone is in the early stages of cracking, and a certain proportion of SMG is detected. In the south-mid sub-sections of the No. 5

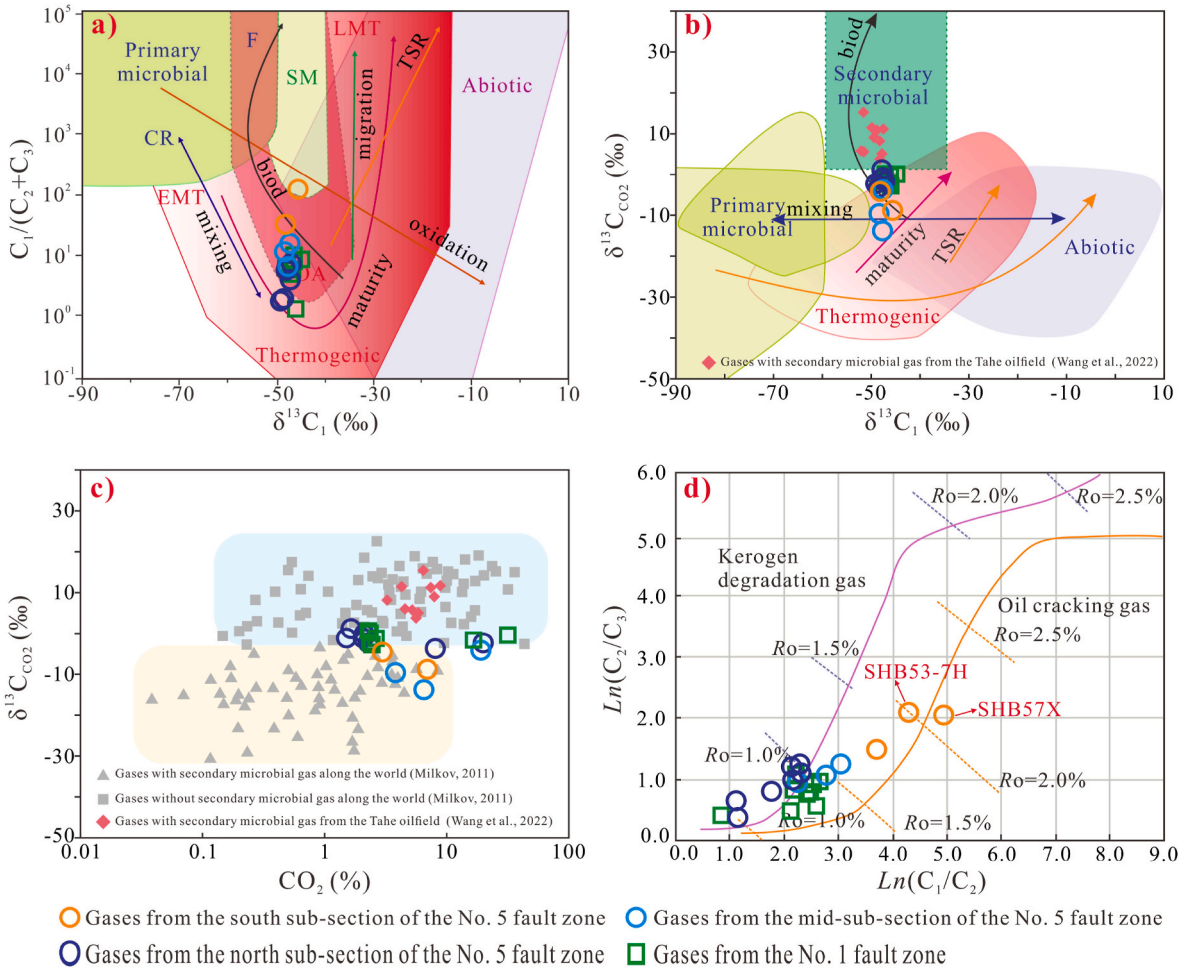

Fig. 18. Cross-plots identify the origin of natural gases from the Shunbei oilfield. a) $C_1/(C_2+C_3)$ versus $\delta^{13}C_1$ (from Milkov and Etiope, 2018); b) $\delta^{13}C_{CO2}$ versus $\delta^{13}C_1$ (from Milkov, 2011); c) $\delta^{13}C_{CO2}$ versus CO_2 (from Milkov, 2011); d) $Ln(C_2/C_3)$ versus $Ln(C_1/C_2)$ (from Li et al., 2017).

fault zone, a large amount of gas has been generated due to the high degree of oil cracking. The high proportion of thermogenic gas obscures the characteristics of SMG (Jautzy et al., 2021).

The cross plot of $Ln(C_1/C_2)$ and $Ln(C_2/C_3)$ indicates that natural gas samples from the No. 1 fault zone and the north sub-sections of the No. 5 fault zone predominantly exhibit the characteristics of kerogen degradation gas. In contrast, the mid-sub-sections of the No. 5 fault zone, along with the two sample points in the south sub-sections of the No. 5 fault zone and the remaining natural gas samples in the No. 1 fault zone, display a transition between kerogen degradation gas and oil cracking gas. Well SHB57X primarily contains oil cracking gas (Fig. 18d). This suggests a gradual transition of natural gas characteristics from kerogen degradation gas in the north to oil cracking gas in the south (Fig. 18d).

5.5. Petroleum accumulation

5.5.1. Fluorescence characteristics of oil inclusions

Hydrocarbon inclusions in the Ordovician Yijianfang Formation in the study area are predominantly found in dissolved pores, fractures, and mold pores in sparry calcite and calcite (Fig. 19). The fluorescence colors of these hydrocarbon inclusions are complex and varied and include yellow-green, blue-green, blue-white, and non-fluorescent (Fig. 19). These variations suggest disparities in crude maturity during capture as well as historical complexity in hydrocarbon filling (Munz, 2001; Ping et al., 2017). At a depth of 7786.00 m in well SHB53–2H, hydrocarbon inclusions containing bituminous material were identified (Fig. 19c). A λ_{max} value of 548 nm and a yellow-green fluorescence color indicate low maturity (Fig. 19c2 and c3). The presence of bitumen suggests potential thermal alteration post-capture (Fig. 19c1).

5.5.2. Petroleum filling period and accumulation process

Examination of the homogenization temperatures of associated brine inclusions and consideration of the burial-thermal history provided the petroleum filling periods and times for the three Ordovician reservoirs—SHB1-3, SHB5, and SHB53–2H (Fig. 20). Well SHB1-3 underwent three periods of hydrocarbon filling during the late Caledonian (435.84–430.70 Ma), Indosinian (235.70–219.34 Ma), and Himalayan (27.19–3.04 Ma) periods (Fig. 20a). Well SHB5 experienced two periods of hydrocarbon filling in the late Caledonian period (436.29–431.20 Ma) and the Indosinian period (240.32–224.44 Ma) (Fig. 20b). Well SHB53–2H experienced three periods of hydrocarbon filling in the late Caledonian (448.21–445.85 Ma), Indosinian (240.98–237.28 Ma), and Himalayan (19.25–12.93 Ma) periods (Fig. 20c). The timing of the first oil filling is basically consistent with the calcite U–Pb dates (447.4–424 Ma) from previous research (Cong et al., 2024). The timing of petroleum filling during the Indosinian and Himalayan periods also aligns closely with previous results (Li et al., 2022a).

The heat flow value reported by Li et al. (2022a) was used to simulate the single-well burial-thermal history. Seismic profiles in the mid-north sub-sections of the No. 5 fault zone showed no significant diabase intrusions, indicating the absence or weakening of hydrothermal activity (Fig. 9c and d). Consequently, the Permian heat flow value for well SHB5 was corrected and adjusted based on the constraint of equivalent vitrinite reflectance, as calculated by bitumen reflectivity (Fig. 20d).

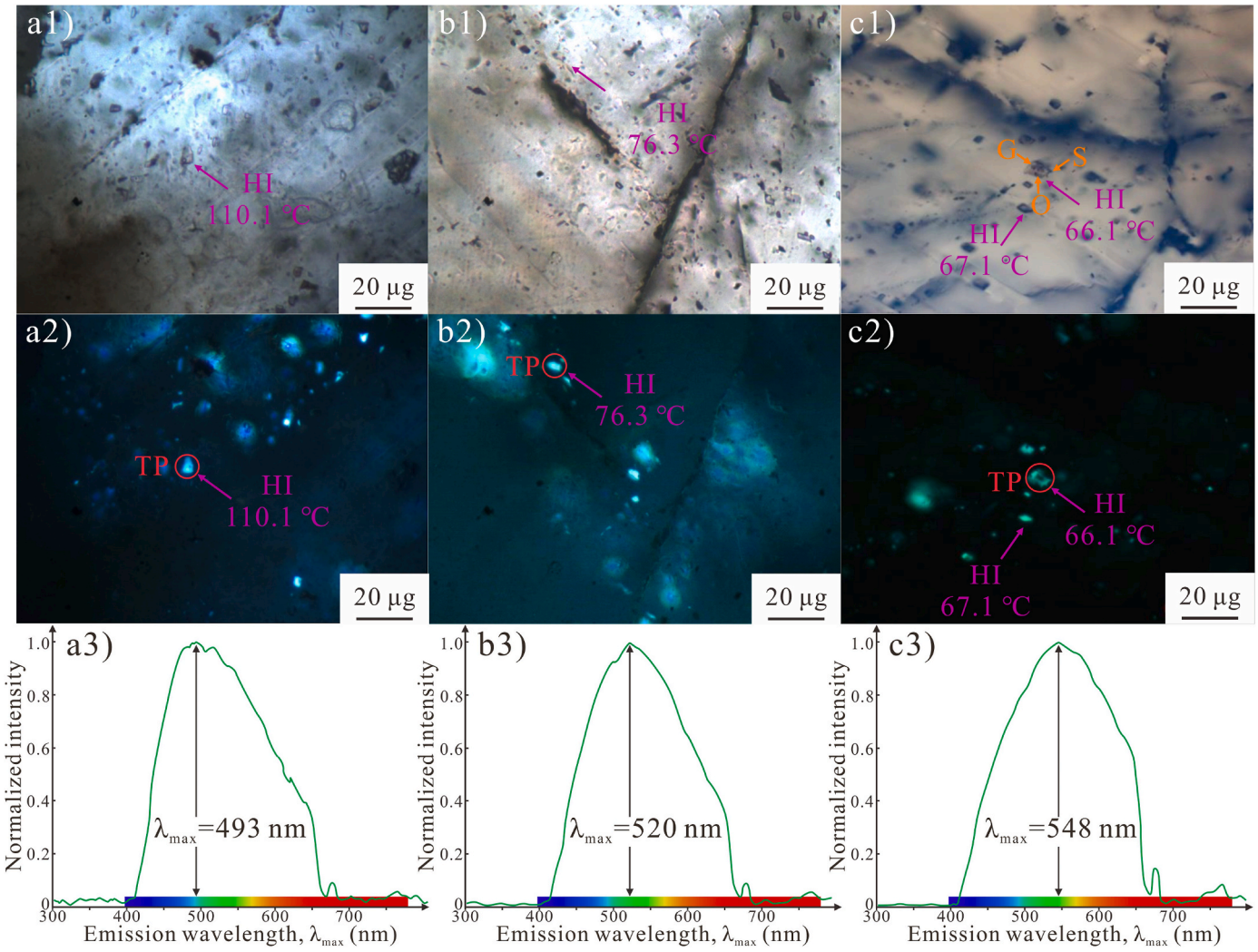

Fig. 19. Microscopic images and fluorescence micro-spectrometry of oil inclusions observed in the Yijianfang (O_2yj) reservoirs of the wells SHB1-3, SHB5, and SHB53–2H. (O: oil; Gas: gas; S: solid bitumen; HI: hydrocarbon inclusion; TP: fluorescence micro-spectrometry test point). a1), b1), c1) are the transmitted light; a2), b2), c2) are the fluorescent; a1), a2) and a3): SHB1-3, O_2yj, 7273.70 m, algal limestone, λ_{max} = 493 nm; b1), b2) and b3): SHB5, O_2yj, 7426.00 m, sparite limestone, λ_{max} = 520 nm; c1), c2) and c3): SHB53–2H, O_2yj, 7786.00 m, grain limestone, λ_{max} = 548 nm.

Analysis of single-well reservoir temperature evolution and hydrocarbon filling showed that the reservoir temperature remained below 80 °C during the first period of oil filling, providing favorable conditions for biodegradation. The presence of 25-NHs in the oil and the mixing of SMG in the natural gas provide additional evidence of biodegradation in the early stages of reservoir formation in the study area (Fig. 6, a3–e3).

The reservoirs within the No. 1 fault zone and the south sub-sections of the No. 5 fault zone were affected by hydrothermal activity during the Permian (290 Ma to 259 Ma), resulting in varying degrees of thermal alteration of the oil during the first stage of accumulation. Well SHB57X was the most affected by hydrothermal activity, as evidenced by extensive biomarker cracking, the rich content of PAHs, unusually heavy carbon isotope values in *n*-alkanes, and the predominance of oil cracking gas (Fig. 6; Fig. 7; Fig. 14; Fig. 16; Fig. 18d).

When hydrothermal activity declined, the formation temperature normalized, initiating the second stage of hydrocarbon filling. Owing to the impact of the earlier hydrothermal activity, the hydrocarbon-generating capacity of the underlying source rocks in the south sub-sections of the No. 5 fault zone declined rapidly. During this period, hydrocarbons likely mostly originated from potential petroleum reservoirs in the Cambrian system. This confirms that TSR occurs in potential Cambrian reservoirs. This also explains the comparatively low temperature of the SHB57X reservoir (163.32 °C) and the lack of strong hydrothermal activity in the late stage, but no biomarkers of the second-stage charged oil have been detected.

The third period of gas filling took place in the No. 1 fault zone and the mid-south sub-sections of the No. 5 fault zone (Fig. 20) during the Himalayan period. Evaporative fractionation reformed the oil from the early stages to form the present gas, condensate, and volatile reservoir. The north sub-sections of the No. 5 fault zone did not experience late gas filling, resulting in the notable predominance of light oil reservoirs.

6. Conclusion

Our analysis of the geochemical characteristics of ultra-deep Ordovician petroleum and hydrocarbon filling events in the Shunbei oilfield yields several key insights:

The light hydrocarbon and diamondoid parameters indicate that the oil in the study area has reached the mature to high mature stage. With an equivalent vitrinite reflectance range of 1.27%–1.60%, the overall trend suggests higher maturity in the south and lower maturity in the north. Carbon isotope and biomarker analyses support a common source for the oil, primarily originating from type II organic matter in a marine-reducing environment. Combining these findings with previous analyses of source rocks and sedimentary facies, it is inferred that the oil in the study area predominantly originates from the Cambrian Yuertusi

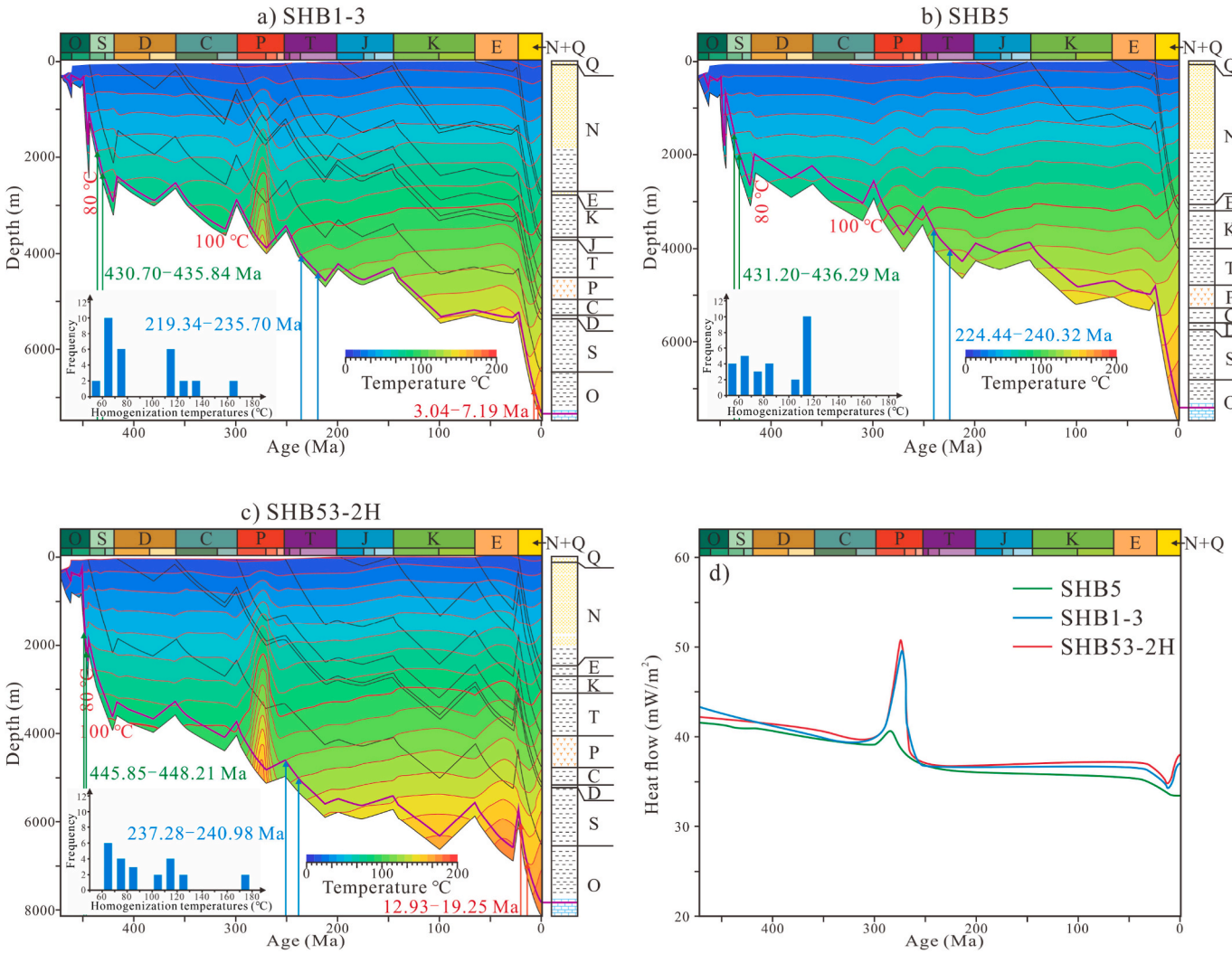

Fig. 20. The buried-thermal (a–c) and heat flow (d) evolution histories of the wells SHB1-3, SHB5, and SHB53–2H.

Formation.

The organic geochemical characteristics of oil, coupled with seismic profile analysis, reveal the influence of biodegradation, oil cracking, thermal alteration, and evaporative fractionation. These secondary effects indicate a multi-stage petroleum mixing process in the oilfield. Additionally, the discrepancy between the values of K_1 and DBTs content suggests the occurrence of thermochemical sulfate reduction reactions in Cambrian potential reservoirs, highlighting the significant petroleum exploration potential of the Cambrian system.

Analysis of the molecular and stable isotopic compositions of natural gas confirms its thermogenic nature, with a minor contribution from secondary microbial gas. From south to north, the natural gas showed a transition trend from oil cracking gas to kerogen degrading gas.

Our findings identify two to three distinct periods of hydrocarbon filling in the region, with the north sub-sections of the No. 5 fault zone having experienced two periods (late Caledonian and Indosinian), while the No. 1 fault zone and mid-south sub-sections of the No. 5 fault zone experienced three periods (late Caledonian, Indosinian, and Himalayan).

Hydrothermal activity during the Permian era rapidly cracked saturated hydrocarbon biomarkers and caused the formation of polycyclic aromatic hydrocarbons in the oil. In addition, evaporative fractionation induced by the differential filling of natural gas during the Himalayan period is shown to have exerted significant control over the distribution of hydrocarbon phases within the study area.

These conclusions provide valuable insights into the complex petroleum system dynamics and hydrocarbon filling history of the Shunbei oilfield, offering essential guidance for future exploration and production in the region.

CRediT authorship contribution statement

Rongzhen Qiao: Writing – review & editing, Writing – original draft, Visualization, Validation, Methodology, Investigation, Conceptualization. **Meijun Li:** Writing – review & editing, Visualization, Supervision, Resources. **Donglin Zhang:** Software, Methodology, Investigation, Formal analysis, Data curation. **Hong Xiao:** Resources, Methodology, Investigation, Formal analysis.

Declaration of competing interest

The authors declare that they have no known competing financial interests or personal relationships that could have appeared to influence the work reported in this paper.

Data availability

Data will be made available on request.

Acknowledgements

This work was funded by the National Natural Science Foundations of China (Grant No. 42173054). The authors gratefully acknowledge the SINOPEC Northwest Company (Urumqi) for sample collection. The author would like to express gratitude to the associate editor, Dr. Miroslaw Slowakiewicz, and the two anonymous reviewers for their valuable and constructive reviews, which have substantially enhanced the manuscript.

References

Alexander, R., Kagi, R.I., Sheppard, P.N., 1983. Relative abundance of dimethylnaphthalene isomers in crude oils. J. Chromatogr. A 267, 367–372.
Amthor, J.E., Grotzinger, J.P., Schröder, S., Bowring, S.A., Ramezani, J., Martin, M.W., Matter, A., 2003. Extinction of cloudina and namacalathus at the precambrian-cambrian boundary in Oman. Geology 31 (5), 431–434.
Bian, J., Hou, D., Cui, Y., Zhu, X., 2023. Geochemical characteristics and origin of the ultra-deep hydrocarbons from the Shunbei Oilfield in the Tarim Basin, China: insight from molecular biomarkers and carbon isotope geochemistry. Mar. Petrol. Geol. 158, 106542.
Brocks, J.J., Buick, R., Summons, R.E., Logan, G.A., 2003. A reconstruction of Archean biological diversity based on molecular fossils from the 2.78 to 2.45 billion-year-old Mount Bruce Supergroup, Hamersley Basin, Western Australia. Geochem. Cosmochim. Acta 67, 4321–4335.
Cai, C., Hu, W., Worden, R.H., 2001. Thermochemical sulphate reduction in cambro–ordovician carbonates in central Tarim. Mar. Petrol. Geol. 18, 729–741.
Cai, C., Dong, H., Li, H., Xiao, X., Ou, G., Zhang, C., 2007. Mineralogical and geochemical evidence for coupled bacterial uranium mineralization and hydrocarbon oxidation in the Shashagetai deposit, NW China. Chem. Geol. 236, 167–179.
Cai, C., Zhang, C., Cai, L., Wu, G., Jiang, L., Xu, Z., Li, K., Ma, A., Chen, L., 2009a. Origins of palaeozoic oils in the Tarim Basin: evidence from sulfur isotopes and biomarkers. Chem. Geol. 268, 197–210.
Cai, C., Li, K., Ma, A., Zhang, C., Worden, R.H., Xu, Z., Wu, G., Zhang, B., Chen, L., 2009b. Distinguishing the Cambrian source rock from the Upper Ordovician: evidence from sulfur isotopes and biomarkers in the Tarim Basin. Org. Geochem. 40, 755–768.
Cai, C., Zhang, C., Worden, R.H., Wang, T., Li, H., Jiang, L., Huang, S., Zhang, B., 2015. Application of sulfur and carbon isotopes to oil–source rock correlation: a case study from the Tazhong area, Tarim Basin, China. Org. Geochem. 83–84, 140–152.
Cai, C., Amrani, A., Worden, R.H., Xiao, Q., Wang, T., Gvirtzman, Z., Li, H., Said-Ahmad, W., Jia, L., 2016. Sulfur isotopic compositions of individual organosulfur compounds and their genetic links in the Lower Paleozoic petroleum pools of the Tarim Basin, NW China. Geochem. Cosmochim. Acta 182, 88–108.
Cao, Z., Ma, A., Xu, Q., Pan, Q., Shang, K., Feng, F., Liu, Y., 2024. Geochemical characteristics and exploration significance of ultra-deep Sinian oil and gas from Well Tashen 5, Tarim Basin, NW China. Energy Geoscience 5 (1), 100217.
Chen, J., Fu, J., Sheng, G., Liu, D., Zhang, J., 1996. Diamondoid hydrocarbon ratios: novel maturity indices for highly mature crude oil. Org. Geochem. 25, 179–190.
Chen, Z., Simoneit, B.R.T., Wang, T.G., Ni, Z.Y., Yuan, G.H., Chang, X.C., 2017. Biomarker signatures of sinian bitumens in the moxi–gaoshiti bulge of Sichuan Basin, China: geological significance for paleo-oil reservoirs. Precambrian Res. 296, 1–19.
Chen, Z., Chai, Z., Cheng, B., Liu, H., Cao, Y., Cao, Z., Qu, J., 2021. Geochemistry of high-maturity crude oil and gas from deep reservoirs and their geological significance: a case study on Shuntuoguole low uplift, Tarim Basin, western China. AAPG (Am. Assoc. Pet. Geol.) Bull. 105 (1), 65–107.
Chen, J., He, D., Tian, F., Huang, C., Ma, D., Zhang, W., 2022. Control of mechanical stratigraphy on the stratified style of strike-slip faults in the central Tarim Craton, NW China. Tectonophysics 830, 229307.
Chen, Z., Qiao, R., Li, C., Wang, D., Gao, Y., 2022. Hydrocarbon generation potential and model of the deep lacustrine source rocks in the Dongying Depression, Bohai Bay Basin. Mar. Petrol. Geol. 140, 105656.
Clayton, C.J., Bjorøy, M., 1994. Effect of maturity on ^{13}C ^{12}C ratios of individual compounds in North Sea oils. Org. Geochem. 21 (6–7), 737–750.
Cong, F., Tian, J., Hao, F., Wang, Q., Kylander-Clark, A.R.C., Cao, Z., 2024. In-situ calcite U-Pb ages and absolute timing of oil charge events: a case study of ultra-deep carbonate reservoirs in the Shunbei oilfield, Tarim basin, Northwest China. J. Asian Earth Sci. 259, 105904.
Coudrain-Ribstein, A., Gouze, P., Marsily, G., 1998. Temperature-carbon dioxide partial pressure trends in confined aquifers. Chem. Geol. 145, 73–89.
Dahl, J.E., Moldowan, J.M., Peters, K.E., Claypool, G.E., Rooney, M.A., Michael, G.E., Mello, M.R., Kohnen, M.L., 1999. Diamondoid hydrocarbons as indicators of natural oil cracking. Nature 399, 54–61.
Dai, J., 1992. Identification and distinction of various alkane gases. Science in China Series B-Chemistry. Life Sciences & Earth Sciences 35, 1246–1257.
Dalziel, I.W.D., 2014. Cambrian transgression and radiation linked to an Iapetus-Pacific oceanic connection? Geology 42, 979–982.
Davies, G.R., Smith, L.B., 2006. Structurally controlled hydrothermal dolomite reservoir facies: an overview. AAPG (Am. Assoc. Pet. Geol.) Bull. 90 (11), 1641–1690.
Du, J., Li, X., Bao, H., Xu, W., Wang, Y., Huang, J., Wang, H., Wangyan, R., Wang, J., 2019. Geological conditions of natural gas accumulation and new exploration areas in the Mesoproterozoic to Lower Paleozoic of Ordos Basin, NW China. Petrol. Explor. Dev. 46 (5), 866–882.
Dutta, S., Bhattacharya, S., Raju, S.V., 2013. Biomarker signatures from neoproterozoic–early cambrian oil, western India. Org. Geochem. 56, 68–80.
Dyman, T.S., Crovelli, R.A., Bartberger, C.E., Takahashi, K.I., 2002. Worldwide estimates of deep natural gas resources based on the U.S. Geological Survey World Petroleum Assessment 2000. Nat. Resour. Res. 11, 207–218.
Fang, X., Deng, B., Geng, A., Liu, S., Wang, P., Xiao, L., Li, Y., Cheng, B., Jiang, W., Wu, L., 2024. Geochemical properties, mechanism of formation, and source of solid bitumen in the Ediacaran Dengying Formation from the central to northern Sichuan Basin, China. Mar. Petrol. Geol. 159, 106573.
Head, I.M., Jones, M., Larter, S., 2003. Biological activity in the deep subsurface and the origin of heavy oil. Nature 426, 344–352.
Huang, H., Zhang, S., Su, J., 2015. Pyrolytically derived polycyclic aromatic hydrocarbons in marine oils from the Tarim Basin, NW China. Energy Fuels 29, 5578–5586.
Hughes, W.B., Holba, A.G., Dzou, L.I.P., 1995. The ratios of dibenzothiophene to phenanthrene and pristane to phytane as indicators of depositional environment and lithology of petroleum source rocks. Geochem. Cosmochim. Acta 59, 3581–3598.
Hutcheon, I., Abercrombie, H., 1990. Carbon dioxide in clastic rocks and silicate hydrolysis. Geology 18, 541–544.
Jautzy, J.J., Douglas, P., Xie, H., Eiler, J.M., Clark, I.D., 2021. CH_4 isotopic ordering records ultra-slow hydrocarbon biodegradation in the deep subsurface. Earth Planet Sci. Lett. 562, 116841.
Jones, D.M., Head, I.M., Gray, N.D., Adams, J.J., Rowan, A.K., Aitken, C.M., Bennett, B., Huang, H., Brown, A., Bowler, B.F.J., Oldenburg, T., Erdmann, M., Larter, S.R., 2008. Crude oil biodegradation via methanogenesis in subsurface petroleum reservoirs. Nature 451, 176–180.
Justwan, H., Dahl, B., Isaksen, G.H., 2006. Geochemical characterisation and geneticorigin of oils and condensates in the South Viking Graben, Norway. Mar. Petrol. Geol. 23, 213–239.
Kissin, Y.V., 1987. Catagenesis and composition of petroleum: origin of n-alkanes and isoalkanes in petroleum crudes. Geochem. Cosmochim. Acta 51, 2445–2457.
Knoll, A.H., Carroll, S.B., 1999. Early animal evolution: emerging views from comparative biology and geology. Science 284 (5423), 2129–2137.
Krouse, H.R., Viau, C.A., Eliuk, L.S., Ueda, A., Halas, S., 1988. Chemical and isotopic evidence of thermochemical sulphate reduction by light hydrocarbon gases in deep carbonate reservoirs. Nature 333, 415–419.
Li, M., Wang, T., Chen, J., He, F., Yun, L., Akbar, S., Zhang, W., 2010a. Paleo-heat flow evolution of the Tabei uplift in Tarim Basin, northwest China. J. Asian Earth Sci. 37, 52–66.
Li, S., Pang, X., Jin, Z., Yang, H., Xiao, Z., Gu, Q., Zhang, B., 2010b. Petroleum source in the Tazhong Uplift, Tarim Basin: new insights from geochemical and fluid inclusion data. Org. Geochem. 41 (6), 1–22.
Li, S., Amrani, A., Pang, X., Yang, H., Said-Ahmad, W., Zhang, B., Pang, Q., 2015. Origin and quantitative source assessment of deep oils in the Tazhong Uplift, Tarim Basin. Org. Geochem. 78, 531–553.
Li, J., Li, Z., Wang, X., Wang, D., Xie, Z., Li, J., Wang, Y., Han, Z., Ma, C., Wang, Z., Cui, H., Wang, R., Hao, A., 2017. New indexes and charts for genesis identification of multiple natural gases. Petrol. Explor. Dev. 44, 503–512.
Li, D., Chang, J., Qiu, N., Wang, J., Zhang, M., Wu, X., Han, J., Li, H., Ma, A., 2022a. The thermal history in sedimentary basins: a case study of the central Tarim Basin, Western China. J. Asian Earth Sci. 229, 105149.
Li, K., Cai, C., Tan, X., Jiang, H., Fan, J., 2022b. Multiple fluid flow events and diversity of hydrothermal minerals in Neoproterozoic to lower Paleozoic carbonate reservoirs, Tarim Basin, NW China. J. Asian Earth Sci. 233, 105260.
Li, H., Gao, J., Cao, Z., Zhu, X., Guo, X., Zeng, S., 2023. Spatial-temporal distribution of fluid activities and its significance for hydrocarbon accumulation in the strike-slip fault zones, Shuntuoguole low-uplift, Tarim Basin. Earth Sci. Front. 30 (6), 316–328 in Chinese with English abstract.
Liu, S.W., Lei, X., Feng, C.G., Hao, C.Y., 2015. Estimation of subsurface formation temperature in the Tarim Basin, Northwest China: implications for hydrocarbon generation and preservation. Int. J. Earth Sci. 105 (5), 1329–1351.
Ma, Y., Cai, X., Yun, L., Li, Z., Li, H., Deng, S., Zhao, P., 2022. Peirong Practice and theoretical and technical progress in exploration and development of Shunbei ultra-deep carbonate oil and gas field, Tarim Basin, NW China. Petrol. Explor. Dev. 49 (1), 1–20.
Mackenzie, A.S., Patience, R.L., Maxwell, J.R., Vandenbroucke, M., Durand, B., 1980. Molecular parameters of maturation in the Toarcian shales, Paris Basin, France-I. Changes in the configurations of acyclic isoprenoid alkanes, steranes and triterpanes. Geochem. Cosmochim. Acta 44 (11), 1709–1721.
Mango, F.D., 1997. The light hydrocarbons in petroleum: a critical review. Org. Geochem. 26 (7–8), 417–440.
Martín-Martín, J.D., Travé, A., Gomez-Rivas, E., Salas, R., Sizun, J.-P., Vergés, J., Corbella, M., Stafford, S.L., Alfonso, P., 2015. Fault-Controlled and stratabound dolostones in the late aptian–earliest albian benassal formation (maestrat basin, E Spain): petrology and geochemistry constrains. Mar. Petrol. Geol. 65, 83–102.
McCollom, T.M., Seewald, J.S., 2006. Carbon isotope composition of organic compounds produced by abiotic synthesis under hydrothermal conditions. Earth Planet Sci. Lett. 243, 74–84.
Mehay, S., Hashem, M., Rouis, L., Mollianiyazov, E., Bennett, B., Stankiewicz, A., 2021. Understanding lateral and vertical fluid variations in the Pliocene sandstone reservoirs in the eastern South Caspian Basin. AAPG (Am. Assoc. Pet. Geol.) Bull. 105 (11), 2181–2205.

Milkov, A.V., 2011. Worldwide distribution and significance of secondary microbial methane formed during petroleum biodegradation in conventional reservoirs. Org. Geochem. 42, 184–207.
Milkov, A.V., Etiope, G., 2018. Revised genetic diagrams for natural gases based on a global dataset of >20,000 samples. Org. Geochem. 125, 109–120.
Munz, I.A., 2001. Petroleum inclusions in sedimentary basins: systematics. analytical methods and applications 55 (1–4), 195–212.
Ning, F., Yun, J., Zhang, Z., Li, P., 2022. Deformation patterns and hydrocarbon potential related to intracratonic strike-slip fault systems in the east of Central Uplift Belt in the Tarim Basin. Energy Geoscience 3 (1), 63–72.
Orr, W.L., 1974. Changes in sulfur content and isotopic ratios of sulfur during petroleum maturation—study of big horn basin paleozoic oils. AAPG (Am. Assoc. Pet. Geol.) Bull. 58 (11), 2295–2318.
Peng, Y., Cai, C., Fang, C., Wu, L., Liu, D., Sun, P., Liu, D., 2022. Diamondoids and thiadiamondoids generated from hydrothermal pyrolysis of crude oil and TSR experiments. Sci. Rep. 12, 196.
Peters, K.E., Moldowan, J.M., 1993. The Biomarker Guide. Prentice-Hall, New York, p. 363.
Ping, H., Chen, H., Jia, G., 2017. Petroleum accumulation in the deeply buried reservoirs in the northern Dongying Depression, Bohai Bay Basin, China: new insights from fluid inclusions, natural gas geochemistry, and 1-D basin modeling. Mar. Petrol. Geol. 80, 70–93.
Qi, L., 2016. Oil and gas breakthrough in ultra-deep Ordovician carbonate formations in Shuntuoguole uplift, Tarim Basin. China Petroleum Exploration 21, 38–51.
Qiao, R., Chen, Z., 2022. Petroleum phase evolution at high temperature: a combined study of oil cracking experiment and deep oil in Dongying Depression, eastern China. Fuel 326, 124978.
Qiao, R., Chen, Z., Li, C., Wang, D., Gao, Y., Zhao, L., Li, Y., Liu, J., 2022. Geochemistry and accumulation of petroleum in deep lacustrine reservoirs: a case study of Dongying Depression, Bohai Bay Basin. J. Petrol. Sci. Eng. 213, 110433.
Radke, M., Welte, D.H., Willsch, H., 1982. Geochemical study on a well in the Western Canada Basin: relation of the aromatic distribution pattern to maturity of organic matter. Geochem. Cosmochim. Acta 46 (1), 1–10.
Schinteie, R., Brocks, J.J., 2014. Evidence for ancient halophiles? Testing biomarker syngeneity of evaporites from Neoproterozoic and Cambrian strata. Org. Geochem. 72, 46–58.
Schoell, M., 1983. Genetic characterization of natural gases. AAPG (Am. Assoc. Pet. Geol.) Bull. 67, 2225–2238.
Seifert, W.K., Moldowan, J.M., 1978. Applications of steranes, terpanes and monoaromatics to the maturation, migration and source of crude oils. Geochem. Cosmochim. Acta 42 (1), 77–95.
Shanmugam, G., 1985. Significance of coniferous rain forests and related organic matter in generating commercial quantities of oil, gippsland basin, Australia. AAPG (Am. Assoc. Pet. Geol.) Bull. 69 (8), 1241–1254.
Snowdon, L.R., Volkman, J.K., Zhang, Z., Tao, G., Liu, P., 2016. The organic geochemistry of asphaltenes and occluded biomarkers. Org. Geochem. 91, 3–15.
Song, D., Zhang, C., Li, S., Wang, T., Li, M., 2017. Elevated mango's K1 values resulting from thermochemical sulfate reduction within the Tazhong oils, Tarim Basin. Energy Fuels 31, 1250–1258.
Sun, Y., Chen, Z., Xu, S., Cai, P., 2005. Stable carbon and hydrogen isotopic fractionation of individual n-alkanes accompanying biodegradation: evidence from a group of progressively biodegraded oils. Org. Geochem. 36, 225–238.
Thompson, K.F.M., 1983. Classification and thermal history of petroleum based on light hydrocarbons. Geochem. Cosmochim. Acta 47 (2), 303–316.
Thompson, K.F.M., 1987. Fractionated aromatic petroleums and the generation of gas-condensates. Org. Geochem. 11 (6), 573–590.
Volkman, J.K., Alexander, R., Kagi, R.I., Woodhouse, G.W., 1983. Demethylated hopanes in crude oils and their applications in petroleum geochemistry. Geochem. Cosmochim. Acta 47 (4), 785–794.
Wang, Q., Hao, F., Cao, Z., Tian, J., Cong, F., 2021. Geochemistry and origin of the ultra-deep Ordovician oils in the Shunbei field, Tarim Basin, China: implications on alteration and mixing. Mar. Petrol. Geol. 123, 104725.
Wang, D., Cai, C., Yun, L., Cao, Z., Zhang, J., Qi, Y., Liu, J., Jiang, Z., Hu, Y., 2022. Geochemical evidence for secondary microbial gas in deep hot reservoirs of the Tarim Basin. Chem. Geol. 587, 120630.
Wilhelms, A., Larter, S., 2004. Shaken but not always stirred. Impact of petroleum charge mixing on reservoir geochemistry. Geological Society 237 (1), 27–35.
Xu, K., Yu, B., Gong, H., Ruan, Z., Pang, Y., Ren, Y., 2015. Carbonate reservoirs modified by magmatic intrusions in the Bachu area, Tarim Basin, NW China. Geosci. Front. 6 (5), 779–790.
Xu, H., Liu, Q., Zhu, D., Peng, W., Meng, Q., Wang, J., Shi, J., Jin, Z., 2022. Molecular evidence reveals the presence of hydrothermal effect on ultra-deep-preserved organic compounds. Chem. Geol. 608, 121045.
Xu, H., Liu, Q., Jin, Z., Zhu, D., Meng, Q., Wu, X., Li, P., Zhu, B., 2024. Organic compounds in geological hydrothermal systems: a critical review of molecular transformation and distribution. Earth Sci. Rev. 252, 104757.
Yamanaka, T., Ishibashi, J., Hashimoto, J., 2000. Organic geochemistry of hydrothermal petroleum generated in the submarine Wakamiko caldera, southern Kyushu, Japan. Org. Geochem. 31, 1117–1132.
Yao, G., Wu, X., Sun, Z., Yu, C., Ge, Y., Yang, X., Wen, L., Ni, C., Fu, X., Zhang, J., 2018. Status and prospects of exploration and exploitation key technologies of the deep petroleum resources in onshore China. Journal of Natural Gas Geoscience 3 (1), 25–35.
Yunker, M.B., Macdonald, R.W., Vingarzan, R., Mitchell, R.H., Goyette, D., Sylvestre, S., 2002. PAHs in the Fraser River basin: a critical appraisal of PAH ratios as indicators of PAH source and composition. Org. Geochem. 33 (4), 489–515.
Zhu, G., Li, T., Zhang, Z., Zhao, K., Zhang, K., Chen, W., Yan, H., Wang, P., 2020. Distribution and geodynamic setting of the late neoproterozoic– early cambrian hydrocarbon source rocks in the south China and Tarim blocks. J. Asian Earth Sci. 201, 104504.
Zhu, G., Milkov, A.V., Li, J., Xue, N., Chen, Y., Hu, J., Li, T., Zhang, Z., Chen, Z., 2021. Deepest oil in Asia: characteristics of petroleum system in the Tarim basin, China. J. Petrol. Sci. Eng. 199, 108246.